Inertial loads on a finite-length cylinder embedded in a steady uniform flow

Nicolas Fintzi, Lionel Gamet ⬤, and Jean-Lou Pierson[*]

IFP Energies Nouvelles, Rond-point de l'échangeur de Solaize, 69360 Solaize, France

Direct numerical simulations are performed to evaluate the hydrodynamic forces and torque on finite-length cylinders embedded in a uniform flow for a wide range of aspect ratios ($2 \leqslant \chi \leqslant 30$). Both viscous-dominated and moderately inertial regimes are investigated. We start the investigation by comparing the numerical results to the predictions of the Khayat and Cox [J. Fluid Mech. **209**, 435 (1989)] slender-body theory. We show that this theory can predict with reasonable accuracy the drag force on the cylinder for a large range of aspect ratios. However, the theory is unable to predict accurately the lift force and torque for moderately long cylinders of $\chi < 30$. By performing a careful analysis of the local contributions to the loads, we show that the disagreement with the theory is mainly explained by the contribution of the cylinder ends which are not properly taken into account by the theory. Semiempirical models based on theoretical results for small but finite inertia are then built to provide a better match with the numerical predictions. We show as in the slender-body theory that the relevant Reynolds number is based on the particle length. We also derive a ready-to-use tensorial formulation for the forces and inertial torque. Additionally, we compare the whole model to experimental results of settling cylinder showing better agreement than the slender-body theory.

I. INTRODUCTION

Microplastic rods or fibers are one of the main classes of microplastic found in the environment due to their wide range of possible sources: synthetic fibers from clothes during washing, fragmentation of maritime equipment, and so on [1]. Due to the large scale involved in the environment, the surrounding flow is essentially turbulent while the microplastic size range from a few micrometers to a few hundred. Because the fully resolved simulation of the overall problem is very challenging from a computational point of view, the motion of anisotropic particles in turbulent flows is most often modeled [2,3]. Such modeling requires the knowledge of the loads acting on the body. In particular, the forces and torque acting on the body due to an incoming uniform flow are required.

The slender-body theory provides a convenient framework to estimate the loads on slender cylinders embedded in a uniform flow. The slender-body theory for Stokes flow was initially developed by Batchelor [4] and Cox [5] (see also the reference therein). In the Stokes flow regime, because of the reversibility of the governing equations, the torque on an axisymmetric cylinder with fore-and-aft symmetry immersed in a uniform flow is zero. However, for finite Reynolds number, a nonzero torque exists when the body is not aligned or perpendicular to the incoming flow [6]. A major breakthrough in extending the slender-body theory to the inertial realm was done by Khayat and Cox [7]. They extended it to small but finite Reynolds numbers based on the body cross-section. In particular, their results allow the computation of the loads for arbitrary Reynolds numbers based on the body length as long as the body aspect ratio is sufficiently large. More recently, Khair and

---

*jean-lou.pierson@ifpen.fr

Chisholm [8] extended the work of Khayat and Cox [7] by calculating the next order inertial term for the force on a fiber embedded in an axisymmetric flow. Despite this progress, one of the main drawbacks of the theory is the inherent limitation due to the slender-body assumption.

Experiments have been carried out to address the range of validity of Khayat and Cox [7] slender-body theory for finite-length fibers and finite-Reynolds numbers. Lopez and Guazzelli [9] studied the settling of inertial fibers in vortical flows. They found good agreement between the Khayat and Cox [7] slender-body theory and their experimental results for aspect ratio χ (defined as the length-to-diameter ratio) of order ten, and particle Reynolds number based on the body half-length Re_L of order 10. Roy *et al.* [10] considered the settling of asymmetric fibers. They also found good agreement with Khayat and Cox [7] torque model for $\chi \geqslant 20$ and $Re_L \geqslant 1$. More recently, Cabrera *et al.* [11] investigated experimentally the settling of slender-cylinder finding good agreement with the theory but better agreement with spheroid models. In parallel, numerical computations have been also carried out addressing properly the inertial flow past a cylindrical particle. Vakil and Green [12] performed direct numerical simulations mainly in the inertial regime. They derived appropriate correlations for predicting the loads on the body. Kharrouba *et al.* [13] performed direct numerical simulations from creeping flow to inertia dominated flow of the same problem for a large range of aspect ratio $1 \leqslant \chi \leqslant 10$, but moderately inclined cylinder. They found good agreement with Khayat and Cox [7] torque model for $\chi \geqslant 5$ and $Re_L \approx 1$.

A consequent amount of work has been devoted to evaluating [7] theory. However, most of the experimental works considered sedimenting particles which has one major drawback when being compared to the theory: the orientation of the cylinder can change with time which may lead to unsteady effects. To compare their experimental results to the theory, most researchers rely on the quasisteady assumption, disregarding any unsteady terms such as added mass effects, history forces or torque, as well as the particle inertia. Although the quasisteady assumption has been discussed and justified *a priori* using scaling arguments [6,10], very little studies are dedicated to assess its range of validity [14]. Moreover, previous works neglect the coupling between translation and rotation which leads to a nonzero lift force [6]. Hence, there is a need for reconsidering the original configuration of Khayat and Cox [7], i.e., the steady uniform flow past a slender cylinder.

The purpose of this paper is twofold. First, we perform a careful numerical analysis of the range of validity of the Khayat and Cox [7] theory. Second, we provide accurate semiempirical formulas based on the numerical simulations and slender-body theory for the drag forces, lift forces and pitching torque for arbitrary yaw angles θ and a wide range of aspect ratios ($2 \leqslant \chi \leqslant 30$), from creeping flow regime to moderate inertial regimes ($0.025 \leqslant Re \leqslant 10$). The development of empirical models serves two main purposes. First, it addresses the practical issue of providing accurate expressions for hydrodynamic loads, which are required for the implementation of Euler-Lagrange models. Second, it supports the current research on the settling behavior of cylindrical particles, where precise expressions for hydrodynamic loads are necessary to distinguish the effect of various contributions, such as unsteady contributions and the coupling between translation and rotation. In Sec. II we describe the problem at hand and the numerical methodology. Then in Sec. III we review the theoretical predictions of the slender-body theory of Ref. [7] compared to the numerical simulations. We investigate in Sec. IV the distribution of the stress on the surface of a cylinder of arbitrary aspect ratios to show from which part of the cylinder the discrepancy with Ref. [7] theory comes from. In Sec. V we propose semiempirical formulas, for the drag, lift and torque. We summarize our results in Sec. VI and compare the proposed model to experimental results for a settling cylinder.

II. COMPUTATIONAL METHODOLOGY

We consider a cylinder of length L and diameter D embedded in a stationary uniform flow of velocity $\mathbf{U} = U\mathbf{e}_x$ (Fig. 1). The cylinder is inclined with an angle θ with respect to the flow direction $\mathbf{e}_x$. The cylinder orientation is also characterized by $\mathbf{p}$ the unit vector along its symmetry axis. The problem is governed by three dimensionless numbers, the Reynolds number, based on the cylinder
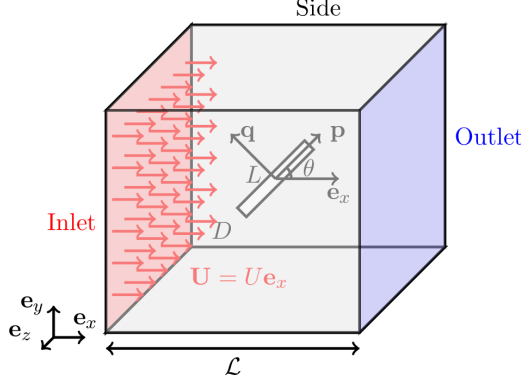
FIG. 1. Scheme of the computational domain.

diameter $\text{Re} = \rho D U / \mu$, the aspect ratio of the cylinder $\chi = L/D$, and the angle of incidence θ. To obtain the load on the body, we solve the steady incompressible Navier-Stokes equations which read

$$\boldsymbol{\nabla} \cdot \mathbf{u} = 0, \tag{1}$$

$$\boldsymbol{\nabla} \cdot (\mathbf{uu}) = -\frac{1}{\rho} \boldsymbol{\nabla} p + \frac{\mu}{\rho} \nabla^2 \mathbf{u}, \tag{2}$$

where μ is the dynamic viscosity, ρ the density, $\mathbf{u}$ the fluid velocity vector, p the fluid pressure. Equations (1) and (2) are solved thanks to the `simpleFOAM` algorithm implemented in the open-source library OpenFOAM [15]. This solver is based on the well-known `SIMPLE` algorithm, which stands for semi-implicit method for pressure-linked equations. A relaxation factor is used on all variables to stabilize the solution at each iteration. It was found that the most efficient relaxation factor for the range of Reynolds numbers studied here was around 0.9. The choice of the finite-volume spatial discretization schemes was obtained after a thorough investigation of their respective accuracy. More details can be found in Fintzi [16] and in Appendix A. In brief, the gradient operator is discretized by using a Gauss linear scheme with second-order accuracy. The divergence operator is discretized using a Gauss integration with linear interpolation (Gauss linear) which is also second-order accurate, while the Laplacian term is discretized by a Gauss linear corrected scheme.

In the low Reynolds numbers regime, one may expect that the velocity field disturbances generated by a cylinder embedded in a uniform flow decrease very slowly with the distance from its centroid. Indeed, the leading order term of the disturbance field generated by a sphere in a uniform flow decreases as $1/r$ [17]. In the case of a slender-body $L \gg D$, the leading order term of the velocity perturbation near the body is even constant [4]. This makes the smallest Reynolds-number simulations particularly costly because of the large domain size [18].

Hence, special care is given to the choice of both the domain size and the boundary conditions to avoid any spurious effects on the numerical results. In Appendix A we have compared the effect of various domain sizes and boundary conditions on the accuracy of the results by comparing our numerical results to previous experimental results of Kasper *et al.* [19]. As shown in Appendix A, a cubic numerical domain of length $\mathcal{L} \approx (100 + 5\chi)D$ is sufficient to avoid any effect of the boundaries for the first configuration. Also, since almost no wake appears in the low to moderate Reynolds number limit studied here, the cylinder is located at the middle of the domain. Dirichlet boundary conditions for the velocity are prescribed both on the cylinder and on the inlet. On the outlet, a Dirichlet boundary condition is imposed for the pressure while a zero-gradient is imposed for the velocity. The choice of the side boundary condition for the first configuration is not trivial and various boundary conditions are tested in Appendix A. The one providing the best results is $\partial p / \partial \mathbf{n} = \mathbf{0}$, $\partial \mathbf{u} / \partial \mathbf{n} = \mathbf{0}$, where $\mathbf{n}$ is the outward normal vector.
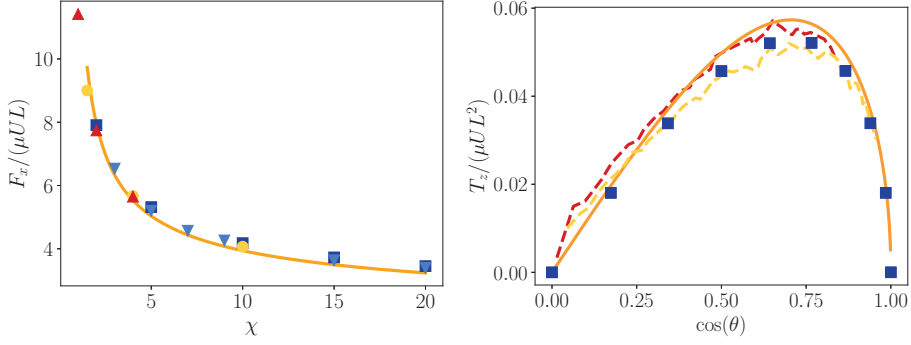
FIG. 2. (Left) Dimensionless drag force F_x on a cylinder held perpendicular to the flow direction for different aspect ratios χ. (Right) Dimensionless torque on a fixed nonrotating cylinder as a function of the inclination angle θ for Re = 0.15 and $\chi = 20$. Dashed lines ($--$): experimental results of Roy *et al.* [10] for settling cylinder Re $\approx$ 0.15; solid line ($-$): [7] slender-body theory [see also Eqs. (B2) and (B4)] at Re = 0 in (left) and Re = 0.15 in (right); blue squares (■) are the present OpenFOAM simulations with Re = 0.025 in (left) and Re = 0.15 in (right); (▲) experimental results of Ref. ; (●) numerical results of Ref. [20]; (▼) experimental results of Kasper *et al.* [19].

The mesh is created using the `snappyHexMesh` utility of OpenFOAM. The background mesh is a fully hexahedral grid created by the `blockMesh` utility. The main criterion for the mesh quality is the number of cells per cylinder diameter near the cylinder surface. We have performed several simulations with increasing density of cells per diameter of cylinders, and we have found a minimum requirement of cells per diameter of 30 for all the Reynolds numbers of interest here. To reduce the computational cost, the characteristic cell size increases as the distance from the body increases. We found out that 20 cells of transition between the different levels of refinement (parameter `nCellsBetweenLevels` of `snappyHexMesh`) were enough to preserve the flow structure near the surface of the cylinder. Depending on the aspect ratio, each mesh contained approximately ten to thirty millions cells. For more information regarding the mesh, Appendix A detailed a careful validation of the mesh generated using `snappyHexMesh` compared to a fully hexahedral mesh.

To further validate our simulations, we performed a comparison with previous experimental and numerical works of the literature. As shown in Fig. 2 (left), our results obtained a very good agreement for the drag force with numerical and experimental data from the literature together with the theory of Ref. [7]. Therefore, this comparison demonstrates that our simulations accurately describe the dynamics in low inertia regime. Additionally, Fig. 2 (right) displays the torque on a fixed nonrotating cylinder with a varying inclination. We have compared our results to the experimental results carried out by Roy *et al.* [10] for a single-cylinder settling under gravity. They measured the translational and angular velocity on a sedimenting cylinder with a high aspect ratio at a low Reynolds number ($\chi = 20$ and Re = 0.156) and based on the quasisteady assumption, they were able to compute the inertial torque. In their original article, Roy *et al.* [10] provided the torque as a function of the angle between the cylinder axis and the gravity vector noted ϕ here. In the present work, the torque is a function of the angle between the incoming velocity (or the particle velocity) and the cylinder axis. A straightforward change of coordinate is thus needed. Roy *et al.* [10] provided the components of the translating velocity at each angle ϕ. Using simple geometrical manipulations one can show that $\cos\theta = (U_v \cos\phi + U_h \sin\phi)/|\mathbf{U}|$ where U_v and U_h are the vertical and horizontal velocity in their original paper. As shown in Fig. 2, a very good agreement is found between the experimental and numerical results. This is noteworthy since the inertial torque is a small quantity in this regime due to its inertial nature, which thus needs an accurate description of the hydrodynamics. Besides, the theory of Ref. [7] happens to agree with the experimental results

and the simulation for both, the drag force and the torque. This point will be discussed further in the next section.

III. COMPARISON WITH SLENDER-BODY THEORY

In this section, we compare the numerical results to Khayat and Cox [7] slender-body theory, which includes small but finite inertia effect. Then, we investigate in more detail the location of the stress on the cylinder.

In their original paper, Khayat and Cox [7] assumed that the Reynolds number based on the body diameter is small but finite (Re $\ll 1$) while the Reynolds number based on the body length is smaller than $\ln(\chi)$. They performed an asymptotic expansion in $1/\ln(\chi)$ assuming that $\chi \gg 1$. In the following, we compare our numerical results for the drag force, the lift force and the inertial torque to their asymptotic results, which are summarized in Appendix B 1. We consider the following range of dimensionless parameters: $0.025 \leqslant \text{Re} \leqslant 10$, $0° \leqslant \theta \leqslant 90°$, and $5 \leqslant \chi \leqslant 30$. We do not show the cases with an aspect ratio $\chi < 5$ since they are obviously out of the range of Khayat and Cox [7] slender-body theory hereinafter called SBT.

Figure 3 shows the numerically obtained drag force, lift force, and torque as well as the prediction of SBT. One can observe that the loads dependency in θ follow simple trigonometric expressions, even in the moderately inertial regime. This point will be discussed further in Sec. V. Figure 3 also shows that the dimensionless drag force matches well the predictions made by the SBT up to Re = 1, even for the lowest aspect ratios considered. For higher Reynolds numbers, the error starts to increase (higher Re greater than 10 can be found in Fintzi [16]).

The SBT lift force predictions, however, are much less accurate than the drag. Even at the smallest Reynolds numbers, the predictions are more than 50% higher than the numerical results for the smallest aspect ratio. Nevertheless, we can still observe that the error decreases with increasing χ. The simulations results show that the dimensionless lift force is almost constant as a function of χ, no matter the value of the Reynolds numbers or the aspect ratio, while the dimensionless force based on SBT behaves as $1/\ln(\chi)$ at the lowest order. Additionally, we remark a minor asymmetry as a function of θ observed at Re = 10. The amplitude of the asymmetry seems to grow with the aspect ratio while the local minimum of the dimensionless lift force stays at $\theta = 50°$. For the pitching torque at Re = 0.025, the SBT provides a good estimation of the torque only for the highest aspect ratio. The SBT is also found to be highly inaccurate at Re $\geqslant 1$, and reveals asymmetric behavior as a function of θ for $\chi \geqslant 10$, while the simulations show this phenomenon at a much higher Reynolds number [13,16]. As the SBT is not meant to be valid for Re > 1, it is not surprising that the inertial terms result in wrong prediction, which is also the case for the dimensionless drag force prediction. We can also notice that at low Reynolds numbers the dimensionless torque increases with the aspect ratio, while for larger Reynolds numbers (Re $\geqslant 1$) the dimensionless torque decreases with the aspect ratio. This phenomenon is qualitatively well described by the SBT even if it cannot quantitatively reproduce the numerical results. To address in more details the error made using the SBT as a function of the dimensionless numbers, we have plotted the relative error for the lift, drag, and pitching torque as a function of the Reynolds number based on half of the body length $\text{Re}_L = \rho L U/(2\mu)$; see Fig. 4. We have plotted the values averaged on all incident angles θ except for $\theta = 0°$ and 90°, since the cylinder experiences no torque nor lift force in these positions. The relative error for the drag force increases considerably after $\text{Re}_L = 2$ and is rather low before. Indeed, for $\text{Re}_L < 2$ the error is below 10% and is nearly independent of χ. For the lift force, we can notice that below $\text{Re}_L \approx 3$ the error is almost constant for a given aspect ratio, and larger than 15% even for the highest aspect ratio. The error behaves nonmonotonically as a function of Re_L. It decreases and then increase for growing Re_L. The same qualitative behavior is observed for the torque.

As a conclusion, to be valid within an acceptable 20% error range, the SBT must satisfy approximately $\chi \geqslant 30$ and $\text{Re}_L \leqslant 10$ for the lift, $\chi \geqslant 30$ and $\text{Re}_L \leqslant 2$ for the torque and $\chi \geqslant 5$ and $\text{Re}_L \leqslant 20$ for the drag force. The large χ requirement for the lift and torque is not surprising
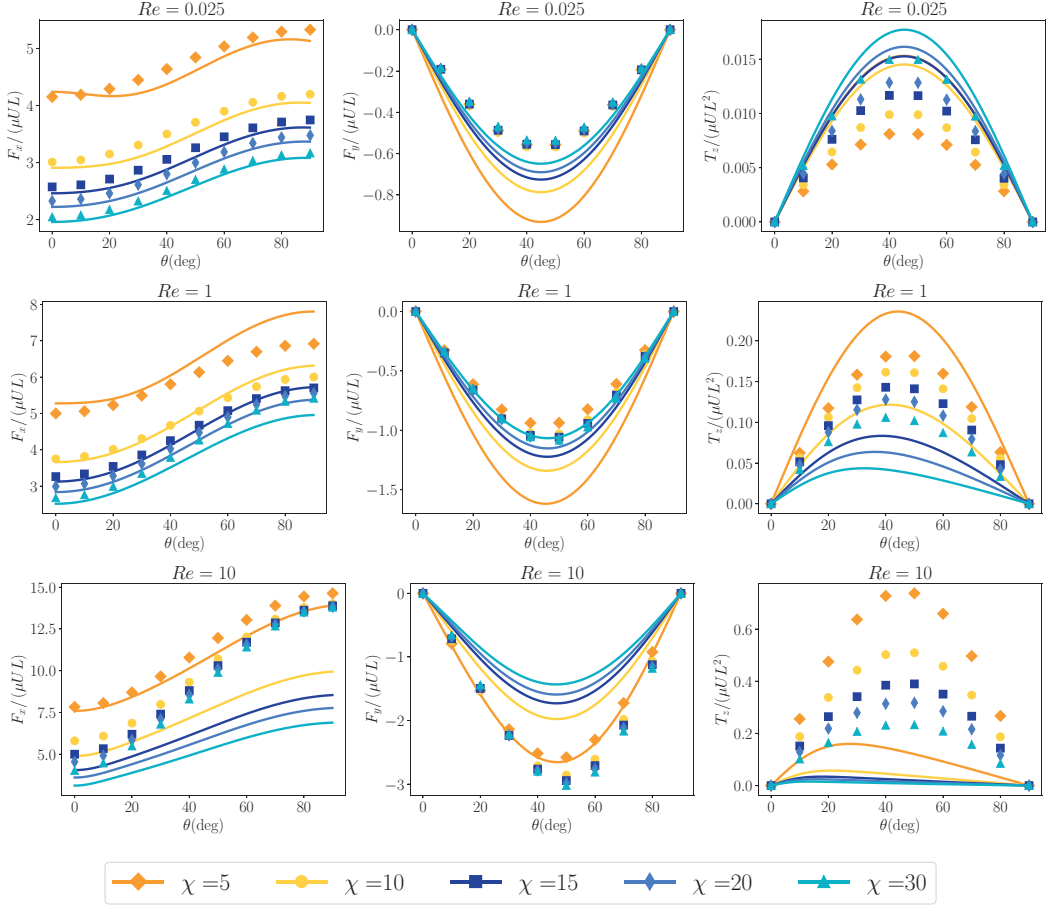
FIG. 3. Dimensionless drag force F_x, lift force F_y and pitching torque T_z on a cylinder versus θ for different aspect ratios and Reynolds numbers. Solid lines: [7] slender-body theory (see Appendix B 1); symbols: present OpenFOAM simulations.
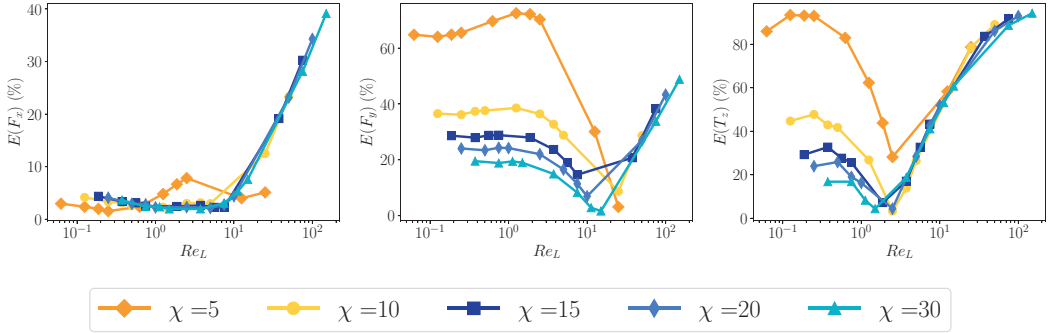

FIG. 4. Mean relative error between the simulations and SBT [see Eqs. (B2), (B3), and (B4)] with respect to Re_L. The mean error is based on an average on all inclination angles and is calculated as $E(F_x) = [\sum_\theta |F_x - F_x^{\text{SBT}}|/F_x]/N_\theta$, where N_θ is the sample of inclination angles. The range of inclination angles is $\theta = 0°$ to $\theta = 90°$ for F_x and $\theta = 10°$ to $\theta = 80°$ for F_y and T_z.

since Khayat and Cox [7] provide an expansion in power $1/\ln\chi$, up to the second term. Moreover, it is important to note that the validity of the SBT is limited to the condition $\mathrm{Re}_L \ll \ln\chi$ [8]. As a result, a very large aspect ratio is needed to reach the assumption required by the theory for finite Re_L. What is less explainable though, is the accuracy of the drag force at low aspect ratios and moderate Re_L. From the present numerical results, one can also note that the agreement between the SBT for the torque and the experimental results of Roy *et al.* [10] ($\mathrm{Re}_L \approx 1.62$, $\chi = 20$) as well as the numerical results of Kharrouba *et al.* [13] for the highest aspect ratio ($\mathrm{Re}_L \geqslant 1$, $\chi = 10$) is partially fortuitous. Indeed, their range of dimensionless parameters are located close to the error local minima in Fig. 4.

IV. LOCAL CONTRIBUTION TO THE LOADS

Although the agreement of SBT with the numerical results for very large aspect ratios is satisfying, we have shown that strong deviations are observed for moderate aspect ratios. This disagreement with the SBT may be explained by investigating the local contribution to the loads. More specifically, what are the load contributions arising from the cylinder ends?

To better understand where the contribution of the total hydrodynamic loads comes from, we investigate in detail the distribution of the stresses over the three different areas of the cylinder surface: the lateral surface, the downstream end, and the upstream end. The lateral surface of the cylinder is denoted "lat," the downstream end "down," and the upstream end "up." A representation of this decomposition is exposed Fig. 5. Such decomposition was already made in Kharrouba *et al.* [13] but for much larger Reynolds numbers. In this section, we consider cylinders with a single inclination $\theta = 40°$, since we have shown in the previous section that the loads' dependency in θ follows simple trigonometric expression, even in moderately inertial regimes. This point will also be discussed in further detail in Sec. V. We can extrapolate results straightforwardly to other inclination angles, except for the singular configurations 0 and 90 degrees. We consider aspect ratios beyond 2 and up to 30. Figure 6 displays the dimensionless loads on each part of the cylinder for two different Reynolds numbers. All contributions are positive for the drag force [Figs. 6(a) and 6(d)]. In the Stokes flow limit, due to the flow reversibility and the body symmetry [17], the contributions from the downstream and upstream ends are equal. We can observe a slight deviation between the downstream and upstream ends for $\mathrm{Re} = 1$ due to the loss of symmetry. Also, the effect of the ends is nonnegligible for moderate χ: its contribution to the total drag is close to 25%. It becomes negligible, with respect to the lateral surface contribution, as χ increases.

The situation for the lift force [Figs. 6(b) and 6(e)] is different since the ends contributions and the lateral contribution have opposite signs. The contribution from the lateral surface is negative while the ends are positive. The combination of these two effects leads to a stronger effect of the ends on the total lift force: not including the ends induces an error of approximately 100% on the lift force for $\chi = 2$. This behavior is also observed for larger Reynolds numbers even if its magnitude is slightly lower. Once again, one can observe that due to the flow reversibility since the contributions of both ends are the same in the Stokes limit while they become different with nonnegligible inertia.

In the limit of zero inertia, the torque on a cylinder is zero due to the reversibility of Stokes equations. This is qualitatively reproduced in Fig. 6(c) for which the lateral contribution is almost zero while the contribution of the ends are opposite. The situation is markedly different for $\mathrm{Re} = 1$
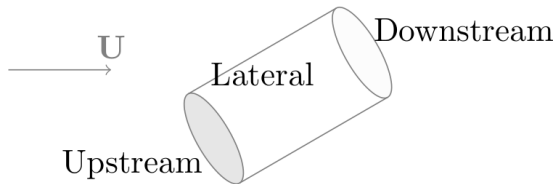

FIG. 5. Scheme of the cylinder's surface decomposition, relatively to the fluid velocity **U**.
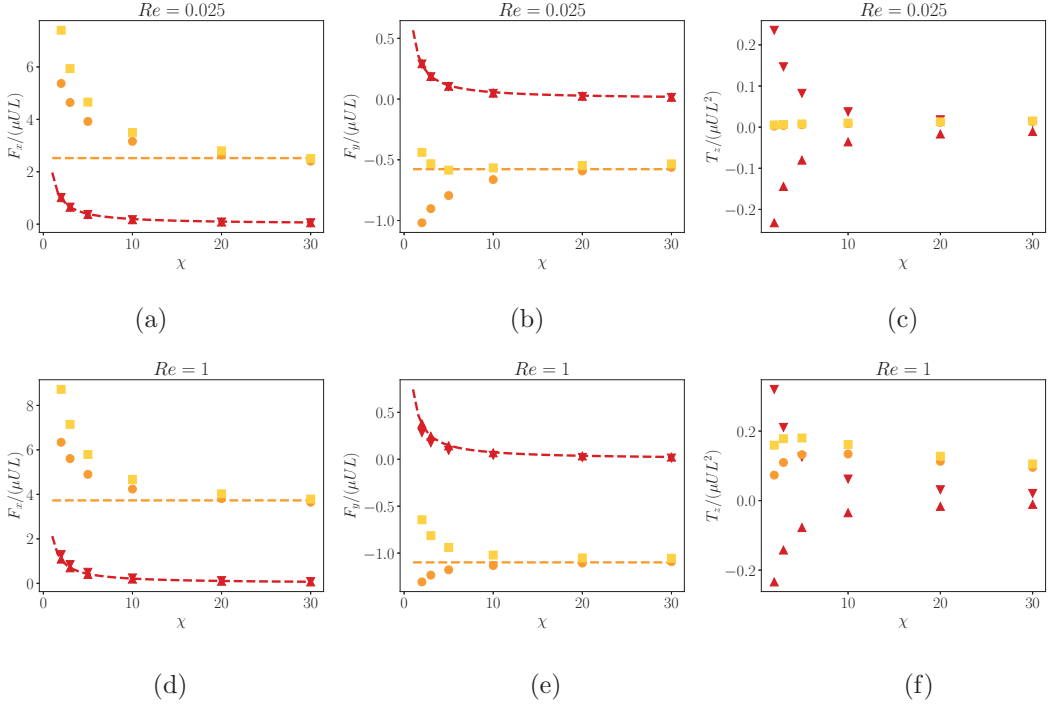
FIG. 6. Contributions to the dimensionless drag force, lift force and torque as a function of χ arising from the lateral and ending surfaces. Two different Re are displayed for a constant inclination $\theta = 40°$. ▼: upstream end; ▲: downstream end; ●: lateral surface; □: sum of all contributions. The dashed lines are fits based on the scaling formulas $\mathbf{F}^{\text{up}}/\mu UL \sim 1/\chi$ and $\mathbf{F}^{\text{lat}}/\mu UL \sim 1$ described in the text.

[Fig. 6(e)]. The lateral surface contribution has a nonmonotonic behavior as a function of χ. As χ increases, it increases for small χ while it starts decreasing for moderate χ. The contribution of the downstream end is more significant than the upstream one, and as a result, the summation of both does not cancel. One can also observe a nonnegligible effect of the ends on the overall contribution with almost 50% contribution for the smallest χ at Re = 1. We can conclude that ends contributions are much larger for the lift force and torque than for the drag force for moderate χ.

The contribution of each surface to the lift and drag forces as a function of χ can be understood by scaling arguments. From the stokes equation, we can assume that the stress σ, pressure or viscous, scale as $\sigma \sim \mu U/D$. Integrating this stress over the surface of interest, one gets the forces acting on each of the surfaces. In particular, $\mathbf{F}^{\text{down}} \sim \sigma D^2 \sim \mu UD$. Hence, $\mathbf{F}^{\text{down}}/\mu UL \sim 1/\chi$ while following the same argument $\mathbf{F}^{\text{up}}/\mu UL \sim 1/\chi$ and $\mathbf{F}^{\text{lat}}/\mu UL \sim 1$. These simple scalings prove to match the numerical data for a large range of aspect ratios (Fig. 6). The scaling for the end contribution matches the numerical data on the whole range of χ while the scaling behavior of the lateral surface is reached for large χ. Although the sum of all contributions in the limit $\chi \gg 1$ and Re $\ll 1$ should scale as $1/\ln(\chi)$ (see SBT), these simple scaling arguments provide a fairly good estimate of the surface force contributions.

Although the previous results help in understanding the ending surface contribution to the loads, which is especially important for the lift force and torque, they cannot explain on their own why the SBT fails for moderate aspect ratio. As explained in Appendix B 1, the SBT relies on the integration over the length of the body of a specific distribution of force per unit of length which allows to quantitatively take into account the shape of the body as well as the singular end since this distribution may diverge. To analyze in greater detail the departure from the SBT, we now focus on
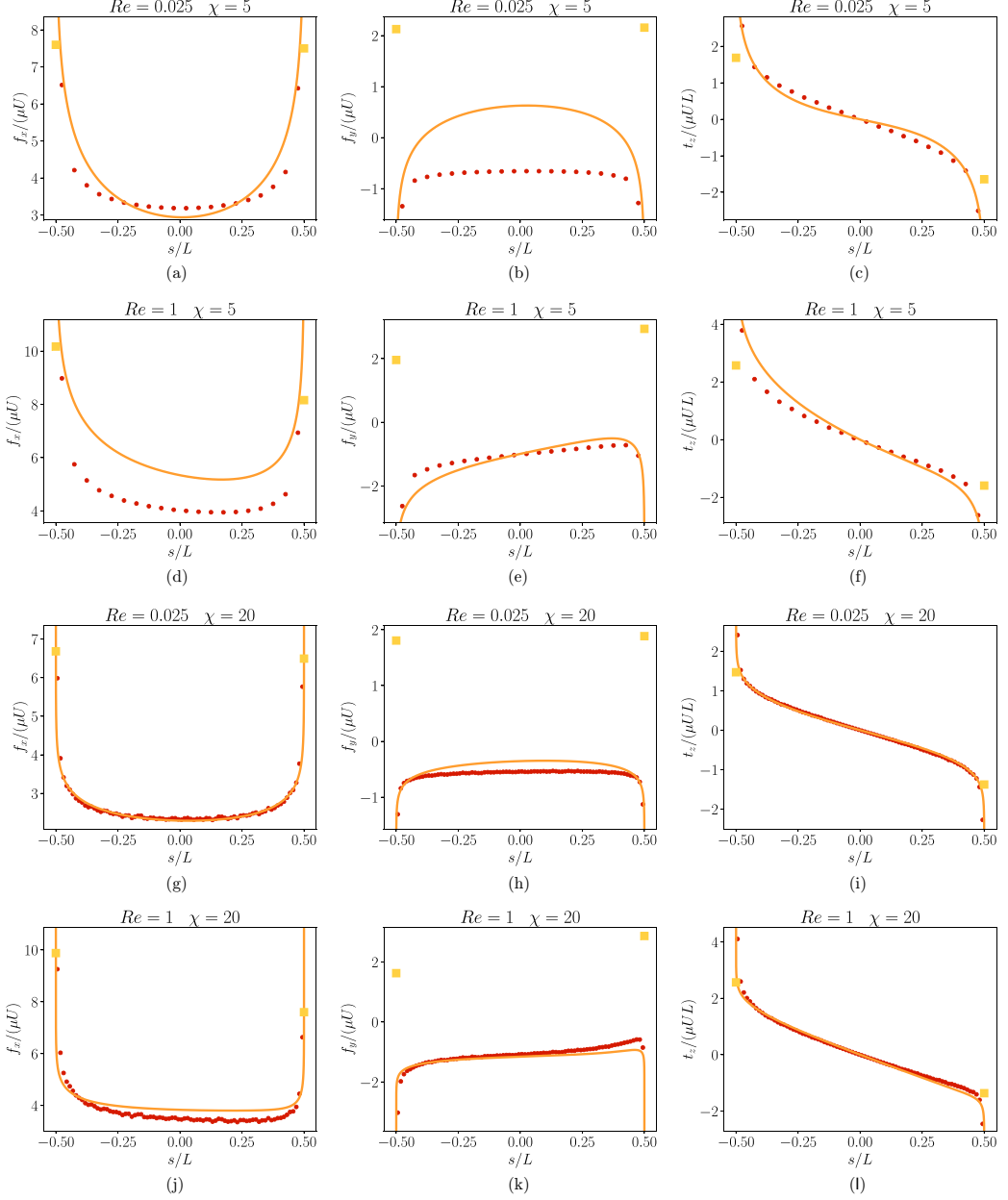
FIG. 7. Dimensionless forces and torque per unit of length for a $\theta = 40°$. s is the axial coordinate along the cylinder axis whose origin is the cylinder centroid. Solid lines: SBT (see Appendix B 1); •: loads on the lateral part; ■: loads on the ending surfaces of the cylinder.

the force density distribution along the axis of the cylinder. To compute this quantity numerically, we divide the cylinder into n slices of length Δh. The two ending surfaces of the cylinder are considered the first and last slice. To conserve the area of each slice we choose $\Delta h = D/4$. We define the forces and torque per unit of length as $\mathbf{f}^i = \mathbf{F}^i/\Delta h$ and $\mathbf{t}^i = \mathbf{T}^i/\Delta h$, where i is the index of the ith slice. Figure 7 shows the distribution of force and torque per unit of length. The first noticeable feature on these plots is the upstream-downstream symmetry of the force, or mirror symmetry for

the torque, for low Reynolds number, which completely disappears as inertia comes into play. One may also notice that SBT predicts singular behavior near this end for all the forces and torque. In Figs. 7(a), 7(d) 7(g), and 7(j) we can observe that the drag force per unit of length is remarkably close to the SBT prediction (except for Re = 1 and $\chi = 5$). The singular end effects are even well predicted by the SBT. The situation is markedly different with the lift force with a strong deviation of the SBT from the numerical results near the ends. One can notice that the two ending disks bring a nonnegligible positive contribution while the SBT predicts (except for Re = 0.025, $\chi = 5$) a negative lift force along the body. This is the main reason for the observed discrepancy between the numerical results and the SBT. Note that the sign of these contributions agrees with Fig. 6. Also, the lateral part of the lift force on the body is not described accurately for $\chi = 5$ and Re = 0.025, which also explains the lack of accuracy of the SBT for moderate χ. The torque results from the asymmetry between the upstream and downstream contribution of the cylinder. This asymmetry is clearly evidenced in Figs. 7(f) and 7(l). As for the lift, the ends do not follow the asymptotic behavior predicted by the SBT, even if the torque along the lateral surface is better predicted.

V. SEMIEMPIRICAL EXPRESSION FOR THE LOADS

In the previous part, we have observed that the SBT is unable to predict accurately the loads on moderately long cylinders embedded in a uniform flow. In this section, we make use of the numerical results and SBT as a basis to create fits for the drag force, lift force and torque. This strategy was already proposed by Kharrouba *et al.* [13], but their study was limited to a small range of θ ($0° \leqslant \theta \leqslant 30°$) and moderate aspect ratio ($\chi \leqslant 10$). Since the derivation of fits that depends on the three dimensionless parameters Re, χ, θ is complex, we apply the following strategy. From Fig. 3, we have observed that the forces and torque acting on the inclined cylinder follow simple trigonometric laws as a function of the inclination angles. Indeed, in the Stokes regime due to the linearity of the equations with respect to the boundary conditions, the force on the body can be linearly related to the incoming velocity as

$$F_p(\text{Re} = 0, \chi, \theta) = 3\pi R_p(\chi)\mu U_p(\theta)L, \tag{3}$$

$$F_q(\text{Re} = 0, \chi, \theta) = 3\pi R_q(\chi)\mu U_q(\theta)L, \tag{4}$$

with F_p and F_q being, respectively, the hydrodynamic force along the axis of the cylinder and the force normal to the axis of the cylinder in the (x, y) plane (see Fig. 1) and $R_p(\chi)$ and $R_q(\chi)$ being, respectively, the principal resistance coefficients in the parallel and normal direction which are both functions of χ [21]. Since $U_p = U \cos\theta$ and $U_q = -U \sin\theta$ the force on an arbitrarily oriented cylinder can be related to the forces acting on the same body for the two angles $\theta = 0°$ and $\theta = 90°$ as

$$F_p(\text{Re} = 0, \chi, \theta) = F_x(\text{Re} = 0, \chi, \theta = 0°)\cos\theta, \tag{5}$$

$$F_q(\text{Re} = 0, \chi, \theta) = -F_x(\text{Re} = 0, \chi, \theta = 90°)\sin\theta, \tag{6}$$

where $F_x(\text{Re} = 0, \chi, \theta = 0°) = 3\pi R_p(\chi)\mu UL$ and $F_x(\text{Re} = 0, \chi, \theta = 90°) = 3\pi R_q(\chi)\mu UL$. We take advantage of this property, which is characteristic of the Stokes regime, and assume that the deviation of this θ profile for moderately inertial regimes is sufficiently small to be estimated in a second step as suggested from Fig. 3 and the results for small but finite inertia presented below. Hence, at first we simply need to estimate $F_x(\text{Re}, \chi, \theta = 0°)$ and $F_x(\text{Re}, \chi, \theta = 90°)$.

Before proceeding further, it is interesting to introduce a generalization of the notation as well as report the results of the small but finite inertia regime. In particular, since $F_i = F_p p_i + F_q q_i$ and $q_i q_j = \delta_{ij} - p_i p_j$ we obtain

$$F_i = 3\pi\mu L R_{ij} U_j, \tag{7}$$

with $R_{ij} = R_p p_i p_j + R_q(\delta_{ij} - p_i p_j)$ being the resistance tensor [21]. Formula (7) has been extended to finite inertial effect $\mathrm{Re}_L \ll 1$ by Brenner and Cox [22] (see also Khayat and Cox [7]),

$$F_i = 3\pi \mu L\big[R_{ij}U_j + \tfrac{3}{16}\mathrm{Re}_L(3R_{ij} - \delta_{ij}R_{kl}e_k e_l)R_{jm}U_m\big], \tag{8}$$

where $\boldsymbol{e}$ is the unit vector in the flow direction (here $\boldsymbol{e} = \boldsymbol{e_x}$). Using the previous formula, one obtains in the present configuration,

$$F_p(\mathrm{Re} = 0, \chi, \theta) = 3\pi \mu U L \cos\theta\big[R_p + \tfrac{6}{16}\mathrm{Re}_L R_p^2 - \tfrac{3}{16}\mathrm{Re}_L \sin^2\theta\big(R_p R_q - R_p^2\big)\big], \tag{9}$$

$$F_q(\mathrm{Re} = 0, \chi, \theta) = -3\pi \mu U L \sin\theta\big[R_q + \tfrac{6}{16}\mathrm{Re}_L R_q^2 - \tfrac{3}{16}\mathrm{Re}_L \cos^2\theta\big(R_p R_q - R_q^2\big)\big]. \tag{10}$$

The previous expressions may also be rewritten as

$$F_p(\mathrm{Re}_L \ll, \chi, \theta) = \cos\theta[F_x(\mathrm{Re}_L \ll 1, \chi, \theta = 0°) + \alpha\mathrm{Re}_L \sin^2\theta], \tag{11}$$

$$F_q(\mathrm{Re}_L \ll, \chi, \theta) = -\sin\theta[F_x(\mathrm{Re}_L \ll 1, \chi, \theta = 90°) + \beta\mathrm{Re}_L \cos^2\theta], \tag{12}$$

where $\alpha = -3/16(R_p R_q - R_p^2)$ and $\beta = -3/16(R_p R_q - R_q^2)$. As the previous analysis is limited to $\mathrm{Re}_L \ll 1$, it justifies our assumption of seeking the deviation from the Stokes-based θ profile in a second step. Moreover, it provides the analytical form of the deviation.

In the $\mathrm{Re}_L \ll 1$ limit, the inertial torque reads [7]

$$\frac{T_z(\theta, \chi, \mathrm{Re}_L)}{\mu U L^2} = \frac{5\pi}{24}\frac{\mathrm{Re}_L}{(\ln\chi)^2}\sin(2\theta). \tag{13}$$

As for the forces, it is convenient to write Eq. (13) in tensorial form. Since, $\sin(2\theta) = 2\epsilon_{jkl}e_k p_l e_i p_i$, one may write

$$T_j = \mu L^2 T_{ij}U_i, \tag{14}$$

with $T_{ij} = 2R_T\epsilon_{jkl}e_k p_l e_i p_i$ and $R_T = T_z(\theta, \chi, \mathrm{Re}_L)/[\mu U L^2 \sin(2\theta)]$.

A. Drag force on a cylinder held parallel to the flow direction

To begin with, we use the semiempirical formula based on the fourth-order slender-body theory for Stokes flow (Re = 0) derived by Kharrouba *et al.* [13] which reads

$$\frac{F_x(\mathrm{Re} = 0, \chi, \theta = 0°)}{2\pi \mu U L} = \frac{A_{\mathrm{Re}=0}^{(1)}}{\ln(2\chi)} + \frac{A_{\mathrm{Re}=0}^{(2)}}{\ln^2(2\chi)} + \frac{A_{\mathrm{Re}=0}^{(3)}}{\ln^3(2\chi)} + \frac{A_{\mathrm{Re}=0}^{(4)}}{\ln^4(2\chi)} + \frac{2.34}{\chi^{2/3}\big(\chi - \tfrac{1}{2}\big)^{1.75}}, \tag{15}$$

where $A_{\mathrm{Re}=0}^{(1)} = 1$, $A_{\mathrm{Re}=0}^{(2)} \approx 0.807$, $A_{\mathrm{Re}=0}^{(3)} \approx 0.829$, $A_{\mathrm{Re}=0}^{(4)} \approx 1.45$ and the last term is an empirical term to extend the validity of the slender-body expansion to moderate χ. Note that the numerator in this term is slightly different from the one originally proposed by Kharrouba *et al.* [13] since it gives better agreement with the numerical results. The exact expression of the coefficients $A_{\mathrm{Re}=0}^{(i)}$ can be found in Kharrouba *et al.* [13]. Although Eq. (15) is valid over a wide range of aspect ratio ($\chi \geqslant 2$) it is limited to Re = 0. Kharrouba *et al.* [13] have proposed semiempirical modifications of this formula based on the results of Khayat and Cox [7] and empirical fitting functions. Here, we take advantage of the recent work of Khair and Chisholm [8] who extended Khayat and Cox [7] work by deriving the third-order inertial correction into the $1/\ln(\chi)$ expansion for axisymmetric flow. As proposed by Khair and Chisholm [8] we explicitly separate the inertial contribution from
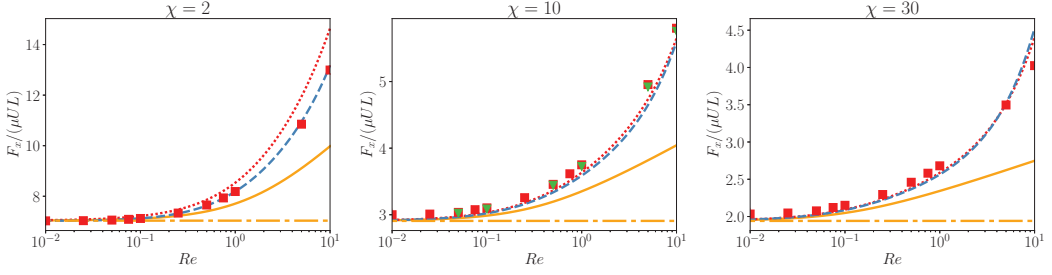
FIG. 8. Drag on a finite-length cylinder aligned with the flow direction versus Re. Dot-dashed lines $(- \cdot -)$: Eq. (15); solid line (—): Eq. (16) with $A^{(3)} = A^{(4)} = 0$; dotted lines $(\cdot\cdot)$: Eq. (16) with $A^{(4)} = 0$; dashed lines (- -): Eq. (16); (■) OpenFOAM simulations; (▼) numerical results of Ref. [13].

the Stokes contribution into the expansion. We seek an expansion of the form

$$
\frac{F_x(\mathrm{Re}_L, \chi, \theta = 0°)}{2\pi \mu U L} = \frac{A_{\mathrm{Re}=0}^{(1)} + A^{(1)}(\mathrm{Re}_L)}{\ln(2\chi)} + \frac{A_{\mathrm{Re}=0}^{(2)} + A^{(2)}(\mathrm{Re}_L)}{\ln^2(2\chi)} + \frac{A_{\mathrm{Re}=0}^{(3)} + A^{(3)}(\mathrm{Re}_L)}{\ln^3(2\chi)}
$$
$$
+ \frac{A_{\mathrm{Re}=0}^{(4)} + A^{(4)}(\mathrm{Re}_L)}{\ln^4(2\chi)} + \frac{2.34}{\chi^{2/3}(\chi - \frac{1}{2})^{1.75}}, \tag{16}
$$

where $A^{(1)}(\mathrm{Re}_L)$, $A^{(2)}(\mathrm{Re}_L)$, $A^{(3)}(\mathrm{Re}_L)$, and $A^{(4)}(\mathrm{Re}_L)$ are functions taking into account finite inertia effects. Note that these functions are functions of Re_L rather than Re, as in the SBT. However, in contrast to Khayat and Cox [7] and Khair and Chisholm [8] who derived expansions in $1/\ln(\chi)$, we have preferred to keep the $1/\ln(2\chi)$ originally proposed by Batchelor [4] since it offers better results. Switching from a $1/\ln(\chi)$ expansion to a $1/\ln(2\chi)$ expansion is straightforward but requires some algebra when higher order terms are considered. The procedure is derived in Appendix B 2. The first-order inertial correction is null, $A^{(1)}(\mathrm{Re}_L) = 0$, while the second-order inertial function reads [7,13]

$$
A^{(2)}(\mathrm{Re}_L) = \frac{1}{2}\left[\frac{E_1(2\mathrm{Re}_L) + \ln(2\mathrm{Re}_L) - e^{-2\mathrm{Re}_L} + \gamma + 1}{2\mathrm{Re}_L} + E_1(2\mathrm{Re}_L) + \ln(2\mathrm{Re}_L) + \gamma - 2\right], \tag{17}
$$

where γ is the Euler constant and $E_1(x) = \int_x^\infty \frac{e^{-t}}{t}dt$ the exponential integral function. In the limit $\mathrm{Re}_L \ll 1$, $A^{(2)}(\mathrm{Re}_L) = \mathrm{Re}_L/4 - \mathrm{Re}_L^2/18 + \mathcal{O}(\mathrm{Re}_L^3)$.

Furthermore, the authors of Ref. [8] have derived an expression for the drag force acting on a slender body immersed in an axisymmetric uniform flow up to the third order. Although [8] derived a force prediction that allows for variations of slender-body shape, they only explicitly considered spheroids. In Appendix B 3 we carry out the derivation for a cylinder, which reads

$$
A^{(3)}(\mathrm{Re}_L) = A_A^{(3)}(\mathrm{Re}_L) + A_B^{(3)}(\mathrm{Re}_L) + 2A^{(2)}(\mathrm{Re}_L) \ln(2), \tag{18}
$$

where the expressions for the first and second terms can be found in Appendix B 3, while the third term appears due to our $1/\ln(2\chi)$ expansion convention. In the limit of small Re_L, $A^{(3)}(\mathrm{Re}_L) = (3/4 - \ln 2/2)\mathrm{Re}_L + (0.215 - 5/54 + \ln 2/9)\mathrm{Re}_L^2 + \mathcal{O}(\mathrm{Re}_L^3)$. This expression provides an analytical expression to this problem up to Re_L^2. For larger Re_L, empirical fits are proposed in Appendix B 3. Figure 8 shows that the third-order inertial correction provides a dramatic improvement for moderate Re_L with respect to the second-order approximation. Nevertheless, it still lacks of accuracy for $\chi = 2$. Thus, to improve the present fit, we propose the following form for the fourth-order
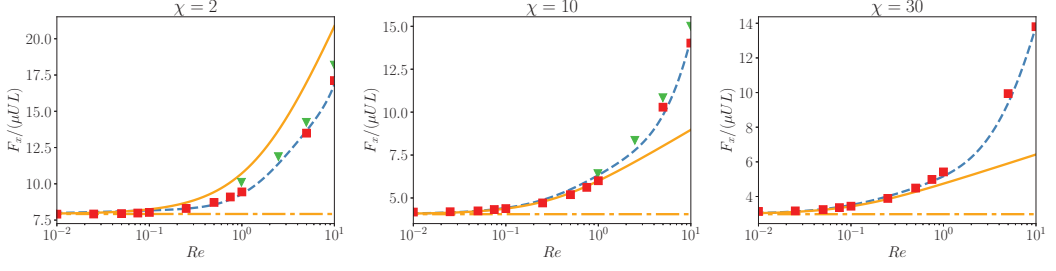
FIG. 9. Drag on a finite-length cylinder perpendicular to the flow direction versus Re. Dot-dashed lines $(-\cdot-)$: Eq. (20); solid line (—): Eq. (21) with $B^{(3)} = B^{(4)} = 0$; dashed lines (- -): Eq. (21); (■) OpenFOAM simulations; (▼) numerical results of Ref. [12].

coefficient

$$A^{(4)}(\text{Re}_L) = 3\ln(2)\big[A_A^{(3)}(\text{Re}_L) + A_B^{(3)}(\text{Re}_L)\big] + 3A^{(2)}(\text{Re}_L)\ln(2)^2 - 0.636\text{Re}_L^{0.762}, \qquad (19)$$

where the first three terms appear due to our $1/\ln(2\chi)$ expansion and the last term is an empirical fitting function. In Fig. 8 we can observe that the final expression of Eq. (16) fit nicely our numerical results. Besides, notice that our results are in total agreement with the simulations of Ref. [13].

B. Drag force on a cylinder held perpendicular to the flow direction

Regarding the drag force on a cylinder at $\theta = 90°$, we apply a similar procedure to that proposed in the previous subsection. Kharrouba *et al.* [13] have derived an expression for a fourth-order expansion term based on slender-body theory for Stokes flow ($\text{Re} = 0$). Their expression can be easily modified to match the numerical results at moderate χ by adding a correction function. It reads

$$\frac{F_x(\text{Re}_L, \chi, \theta = 90°)}{4\pi\mu U L} = \frac{B_{\text{Re}=0}^{(1)}}{\ln(2\chi)} + \frac{B_{\text{Re}=0}^{(2)}}{\ln^2(2\chi)} + \frac{B_{\text{Re}=0}^{(3)}}{\ln^3(2\chi)} + \frac{B_{\text{Re}=0}^{(4)}}{\ln^4(2\chi)} - \frac{0.568}{\chi^{2/3}\big(\chi - \frac{1}{2}\big)^{1.75}}, \qquad (20)$$

where the coefficients $B_{\text{Re}=0}^{(1)}$ can be found in Kharrouba *et al.* [13] and the last term is an empirical factor.

One can observe in Fig. 9 that this equation matches with very good accuracy the numerical results for all aspect ratios and $\text{Re} \leqslant 0.1$. For higher Reynolds numbers, significant deviation appears. Based on the results of the previous section and the theoretical work of Khayat and Cox [7], we seek an expansion of the form

$$\frac{F_x(\text{Re}_L, \chi, \theta = 90°)}{4\pi\mu U L} = \frac{B_{\text{Re}=0}^{(1)} + B^{(1)}(\text{Re}_L)}{\ln(2\chi)} + \frac{B_{\text{Re}=0}^{(2)} + B^{(2)}(\text{Re}_L)}{\ln^2(2\chi)} + \frac{B_{\text{Re}=0}^{(3)} + B^{(3)}(\text{Re}_L)}{\ln^3(2\chi)}$$
$$+ \frac{B_{\text{Re}=0}^{(4)} + B^{(4)}(\text{Re}_L)}{\ln^4(2\chi)} - \frac{0.568}{\chi^{2/3}\big(\chi - \frac{1}{2}\big)^{1.75}}, \qquad (21)$$

where $B^{(i)}(\text{Re}_L)$ are inertial corrections to the Stokes based SBT. As shown by Khayat and Cox [7], $B^{(1)}(\text{Re}_L) = 0$ and

$$B^{(2)}(\text{Re}_L) = E_1(\text{Re}_L) + \ln(\text{Re}_L) - \frac{e^{-\text{Re}_L} - 1}{\text{Re}_L} + \gamma - 1. \qquad (22)$$

This second-order approximation offers better results in moderately inertial regimes ($\text{Re} \leqslant 1$) in comparison to the Stokes law, but it still lacks accuracy for the smallest aspect ratios (see Fig. 9). To the best of our knowledge the third-order inertial terms, B^3, have not been derived theoretically. We
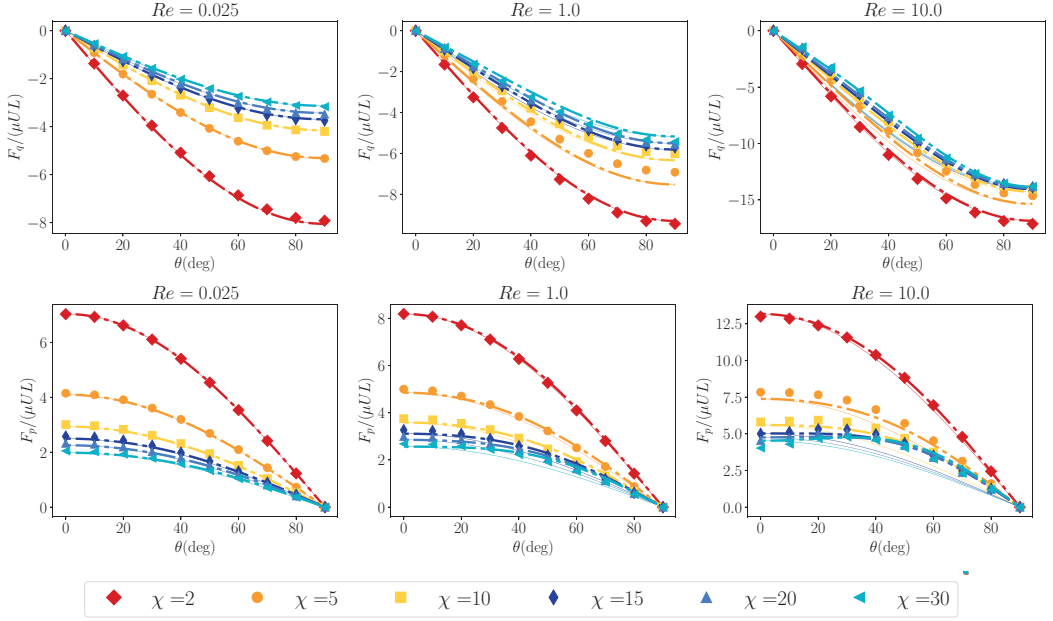
FIG. 10. Parallel and perpendicular forces as a function of the incident angle θ. Symbols: numerical results; solid lines ($-$): Eqs. (25) and (26); dot-dashed lines ($- \cdot -$): Eqs. (27) and (28).

thus search for empirical terms to model the third and fourth-order inertial terms. The best match was obtained with the following functions:

$$B^{(3)}(\mathrm{Re}_L) = 2\ln(2)B^{(2)}(\mathrm{Re}_L) + B_e^{(3)}(\mathrm{Re}_L), \tag{23}$$

$$B^{(4)}(\mathrm{Re}_L) = 3\ln(2)^2 B^{(2)}(\mathrm{Re}_L) + 3\ln(2)B_e^{(3)}(\mathrm{Re}_L) + B_e^{(4)}(\mathrm{Re}_L), \tag{24}$$

where $B_e^{(3)}(\mathrm{Re}_L) = 283.3 e^{-19.799/\mathrm{Re}_L^{0.4211}}$ and $B_e^{(4)}(\mathrm{Re}_L) = -148 e^{-4.376/\mathrm{Re}_L^{0.1829}}$. The addition of these empirical terms provides a significant improvement, especially for the lowest aspect ratios. Moreover, it extends the SBT range of validity to higher Reynolds numbers. The numerical results of Ref. [12] have been also displayed in Fig. 9. One can observe that their results slightly overestimate ours. Also, it is difficult in practice to assess where this discrepancy comes from since the authors are using a different numerical solver. Another possible explanation might be their grid resolution as their simulations used a grid containing 10 times less cells than ours.

C. Forces and torque on an arbitrarily inclined cylinder

In this section, we generalize the above results for any yaw angle θ. We make use of Eqs. (5), (6) and (11), (12) as a basis to derive accurate correlation for any inclination angle. The first possible extension of Eqs. (5) and (6) is to consider that these laws are valid for arbitrary Reynolds number, such as

$$F_p(\mathrm{Re}_L, \chi, \theta) = F_x(\mathrm{Re}_L, \chi, \theta = 0°)\cos\theta, \tag{25}$$

$$F_q(\mathrm{Re}_L, \chi, \theta) = -F_x(\mathrm{Re}_L, \chi, \theta = 90°)\sin\theta, \tag{26}$$

The solid lines in Fig. 10 represent Eqs. (25) and (26) compared to the numerical results. Even though this approximation is not expected to be valid in the inertial regime, it fits reasonably well the behavior of the parallel and perpendicular forces as long as Re $\leqslant 1$ and $\chi \leqslant 10$. For larger
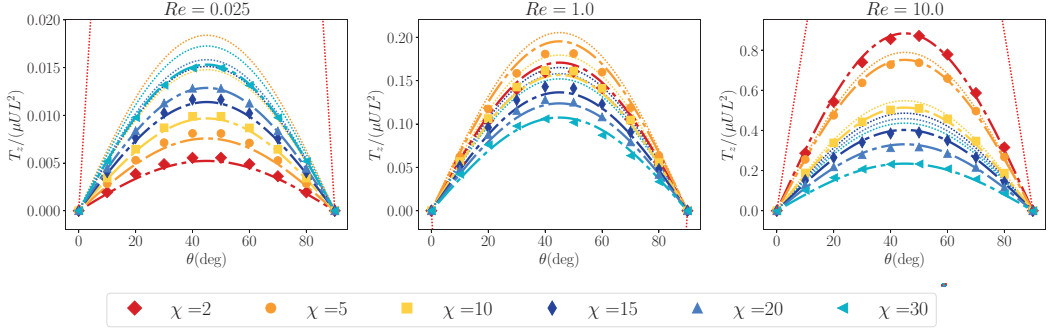
FIG. 11. Inertial torque as a function of θ for different Re. Symbols: numerical results; dotted lines ($\cdots$): semiempirical formula derived by Kharrouba *et al.* [13] [Eq. (30)]; dash-dotted lines ($\cdot - \cdot$): semiempirical formula (31).

Reynolds numbers or aspect ratios, important deviations are observed. Based on Eqs. (11) and (12), which are valid in low inertial regime, we propose the following expressions:

$$F_p(\text{Re}_L, \chi, \theta) = \quad \cos\theta[F_x(\text{Re}_L, \chi, \theta = \ 0°) + G_p(\text{Re}_L)\sin^2\theta], \tag{27}$$

$$F_q(\text{Re}_L, \chi, \theta) = -\sin\theta[F_x(\text{Re}_L, \chi, \theta = 90°) + G_q(\text{Re}_L)\cos^2\theta], \tag{28}$$

where $G_p(\text{Re}_L) = 0.25\mu UL\text{Re}_L^{0.5447}$ and $G_q(\text{Re}_L) = -0.27\mu UL\text{Re}_L^{0.6851}$ are empirical functions, fitted on our numerical results. Equations (27) and (28), represented by the dotted dashed lines in Fig. 10, fit our numerical results over all ranges of parameters considered. Since $\sin^2\theta = q_k e_k q_l e_l$ and $\cos^2\theta = p_k e_k p_l e_l$ the previous formulas can also be generalized to any component of the force by using tensorial notations

$$F_i = \mu L\big(R_{ij}^{\text{Re}} + S_{ij}^{\text{Re}}\big)U_j \tag{29}$$

$R_{ij}^{\text{Re}} = R_p^{\text{Re}} p_i p_j + R_q^{\text{Re}}(\delta_{ij} - p_i p_j)$ is an empiric generalization of the resistance tensor to moderate Reynolds numbers and $S_{ij}^{\text{Re}} = S_p^{\text{Re}}(\delta_{kl} - p_k p_l)e_k e_l p_i p_j + S_q^{\text{Re}} p_k p_l e_k e_l(\delta_{ij} - p_i p_j)$ a second-order tensor taking into account the nonlinear dependency of the force with respect to the incoming velocity. With this definition, the tensor coefficients read $R_p^{\text{Re}} = F_x(\text{Re}_L, \chi, \theta = 0°)/(\mu UL)$, $R_q^{\text{Re}} = F_x(\text{Re}_L, \chi, \theta = 90°)/(\mu UL)$ and $S_p^{\text{Re}} = G_p(\text{Re}_L)/(\mu UL)$, $S_q^{\text{Re}} = G_q(\text{Re}_L)/(\mu UL)$. This tensorial formulation provides a useful framework for the nonresolved computation of particle sedimentation.

D. Modelling the inertial torque

In Sec. III, we concluded that the theoretical formulas of Ref. [7] happen to be inaccurate to describe the inertial torque, except for very large χ. An accurate correlation for moderate χ is needed. Figure 11 shows that the $\sin(2\theta)$ behavior remains valid for all aspect ratios and up to Re = 10. One can also notice the nonmonotonic dependency of the torque with χ (see Fig. 11). This behavior makes the fit of the inertial torque much more complicated than it is for the drag and lift forces. Based on this observation, Kharrouba *et al.* [13] built a semiempirical expression which tends toward the analytical formula as Re_L tends toward zero while being modified by an empirical function for larger Re_L. Their original expression reads

$$\frac{T_z(\theta, \chi, \text{Re})}{\mu UL^2} = \frac{5\pi\sin(2\theta)\text{Re}}{48(1 + \chi\text{Re}^{1.1})^{0.5}}\left[\frac{\chi}{\ln^2(\chi)} + \frac{(13.5 - 30\text{Re}^{0.5})e^{-0.7\text{Re}}}{\chi\ln^3(\chi)}\right]. \tag{30}$$

Their formula matches the numerical results for $0.1 \leqslant \text{Re} \leqslant 10$ and $5 \leqslant \chi \leqslant 15$, which is approximately the range of parameters investigated in their original study. However, it is unable to predict
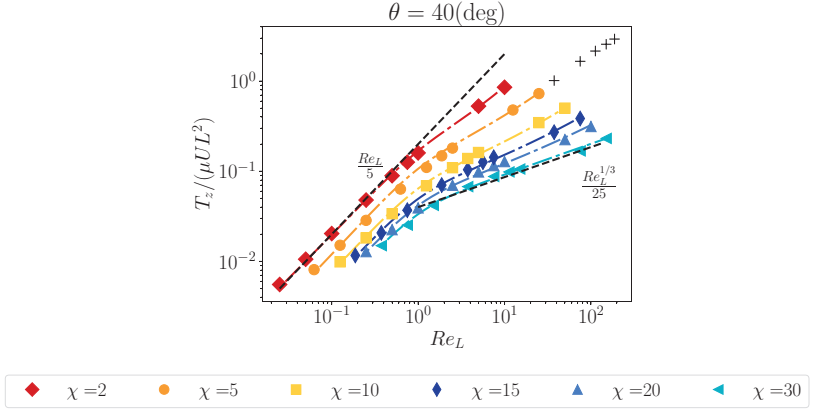
FIG. 12. Inertial torque as a function of Re_L for $\theta = 40^o$. Colored symbols: numerical results; dash-dotted lines $(\cdot - \cdot)$: semiempirical formula (31); crosses (+): numerical results of Pierson *et al.* [23] for $\chi = 3$ and $\theta = 45°$.

the torque with good accuracy for $\text{Re} = 0.025$ and for $\chi \gg 1$ no matter what the value of the Reynolds number is. In the following, we make use of the expression of Kharrouba *et al.* [13] by modifying two important features. First, we notice that the nonmonotonic behavior of the torque can be avoided by expressing it as a function of Re_L rather than Re. Figure 12 displays the dimensionless torque as a function of Re_L for $\theta = 40°$. For a given Re_L the torque decreases monotonically as a function of χ. This confirms that the particle length is the relevant scale as in SBT where the leading order contribution to the torque comes from a volume around the fibre scaling as L^3 [24]. Second, in the same spirit as the drag and lift force formulas, we convert the $1/\ln(\chi)$ expansion into a $1/\ln(3\chi)$ expansion (see Appendix B 2). After adding higher order empirical terms, the expression for the pitching torque which yields the best agreement with the numerical results is

$$\frac{T_z(\theta, \chi, \text{Re}_L)}{\mu U L^2} = \frac{5\pi \sin(2\theta)\text{Re}_L}{24(1 + \text{Re}_L^{1.991})^{0.331}} \left[\frac{1}{\ln^2(3\chi)} + \frac{2.244 - 1.813\text{Re}_L^{0.543}}{\ln^3(3\chi)} \right.$$
$$\left. - \frac{3.603 + 8.854\text{Re}_L^{0.538}}{\ln^4(3\chi)} - \frac{14.301(\text{Re}_L/\chi)^{0.448}}{\ln^5(3\chi)} \right]. \tag{31}$$

A very good match is observed between Eq. (31) and the numerical results (Fig. 11). Finally, it is noteworthy to make some remarks regarding Fig. 12. First, one can observe that the torque Re_L scaling is valid up to $\text{Re}_L \sim 1$ no matter the value of the aspect ratio. For larger Reynolds numbers, the torque still approximately scales as Re_L, for the smallest aspect ratio while for larger ones a much slower increase is observed (close to $\text{Re}_L^{1/3}$). One can also note that for a given Re_L the torque decrease as a function of χ is much stronger than the $1/\ln^2(\chi)$ prediction of the SBT.

VI. DISCUSSION

In this work, direct numerical simulations have been launched to evaluate the hydrodynamical drag force, lift and torque applied to a cylinder immersed in a uniform flow. The numerical results show good agreement with experimental data from several sources giving strong confidence in the numerical methodology. The comparison between the simulations and the extended slender-body theory of Khayat and Cox [7] has shown the limitations of this theory.

The drag force prediction is highly accurate, as we recorded a relative error of less than 5% in the range of $\chi \geqslant 5$ and $\text{Re}_L < 1$. However, this error reaches 40% when considering
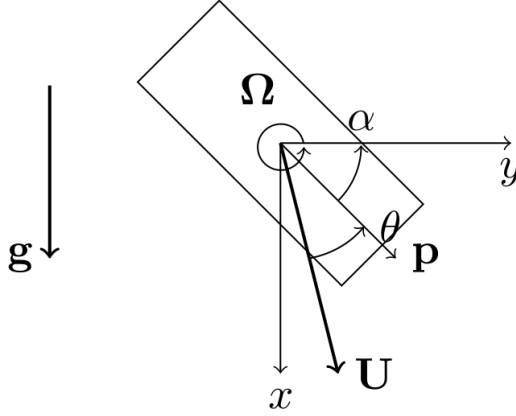
FIG. 13. Finite-length cylinder submitted to the gravity acceleration **g**.

higher Re_L and lower χ. The lift force and torque predictions are considerably less accurate, except for very large aspect ratios. Indeed, for the highest χ considered, the SBT was found to underestimate the lift force and torque to approximately 20%, even in the low inertia regime. Consequently, after providing clear explanations for this inaccuracy, we have built semiempirical formulas to describe with an improved accuracy the force and torque on the body. One question remains to be addressed for the previous expressions to be usable in sedimentation problems: Are the formulas presented here sufficiently accurate to describe the motion of a settling cylinder?

To answer this question, we consider a finite-length cylinder settling under gravity with velocity **U** and angular velocity **Ω** (Fig. 13). We assume that the unsteady particle motion as the cylinder rotates and translates is small. As a result, the motion can be considered quasisteady, and we neglect the particle inertia, history, and added mass loads. Since the time required for the cylinder to change its orientation scales as $1/\Omega$ the previous assumption requires that $\Omega L/U \ll 1$ [6,25]. This requirement may be justified theoretically in the limit $\text{Re}_L \ll 1$ [6]. In practice, experimental results and numerical simulations show that this assumption remains valid up to $\text{Re}_L \approx 1$ [10,11,14]. Still under the limit $\Omega L/U \ll 1$, one may safely neglect the coupling between translation and rotation, and especially the Magnus lift force acting on a translating and rotating body [6,26]. Under this assumption, the body motion is planar. Without loss of generality, we note this plane (x, y), as shown in Fig. 13. Using Eq. (29), the equation of motion reads

$$0 = \mu L\big(R_{ij}^{\text{Re}} + S_{ij}^{\text{Re}}\big)U_j + (\rho_p - \rho)Vg_i, \tag{32}$$

$$0 = T_\Omega + T_i, \tag{33}$$

where ρ_p and V are, respectively, the cylinder density and volume, T_i is the inertial torque whose expression can be found in Sec. V D and T_Ω is the hydrodynamic torque resisting rotation. In contrast to Roy *et al.* [10] and Cabrera *et al.* [11] who used the leading order term in the slender-body expansion for this torque, we used the expression derived by [26] which goes up to the fourth-order of the slender-body expansion and had been validated using direct numerical simulations.

To validate the model, we have compared it to the experimental results of Cabrera *et al.* [11] for settling cylinders with $\text{Re}_L \leqslant 0.4$. Figure 14 displays the results of the model. A very good match with the experimental results is observed for the vertical and horizontal velocities. This is in contrast with the original prediction of the slender-body theory which overestimates the vertical velocity. The agreement for the angular velocity is also very good for the largest aspect ratio, but deviation can be noticed for the smallest one at $\chi = 8$. It is however difficult to assess if
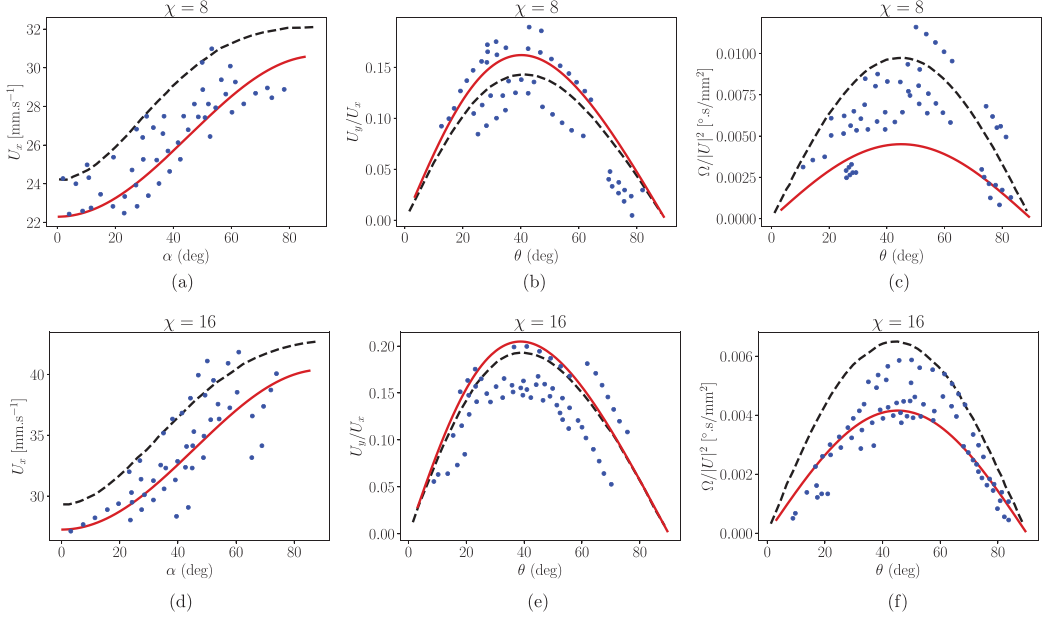
FIG. 14. [(a), (d)] Vertical velocity U_x as a function of the angle α. [(b), (e)] Ratio between horizontal U_y and vertical velocity as a function of θ. [(c), (f)] Angular velocity divided by the square of the velocity. (●): Experimental results from Cabrera *et al.* [11]; solid line (–): present model [Eqs. (32) and (33)]; dashed line (- -): Cabrera *et al.* [11] model based on the SBT. The angle θ and α are defined in Fig. 13.

this discrepancy is due to the present model or to the large scattering of the experimental data. Finally, the present results corroborate the use of the quasisteady assumption in Cabrera *et al.* [11] configuration ($\mathrm{Re}_L \leqslant 0.4$). More work is needed in this regime to properly assess when the quasisteady assumption fails (as a function of χ and Re_L). In particular, the influence of the coupling between rotation and translation on the steady loads may be of particular interest. In a recent paper, Teng *et al.* [27] have performed accurate simulation of the coupling of translation and rotation in the motion of cylindrical rods near solid boundaries. To the best of our knowledge, the equivalent problem without the influence of a solid boundary has not been studied so far and is a matter of future research.

APPENDIX A: VALIDATION OF THE NUMERICAL METHODOLOGY

As mentioned within the text body, the computation of the hydrodynamic stress applied on the sharp surface of a cylinder requires special care. In this Appendix, we investigate the loads' dependence on the mesh definition with meticulous attention. For this purpose, we present several studies where we investigate the mesh refinement, the domain size dependence, the overall mesh topology and the numerical scheme used to discretize the gradient operator. It should be noted that our emphasis is on the discretization of the gradient term as it is the most predominant in the viscous regime.
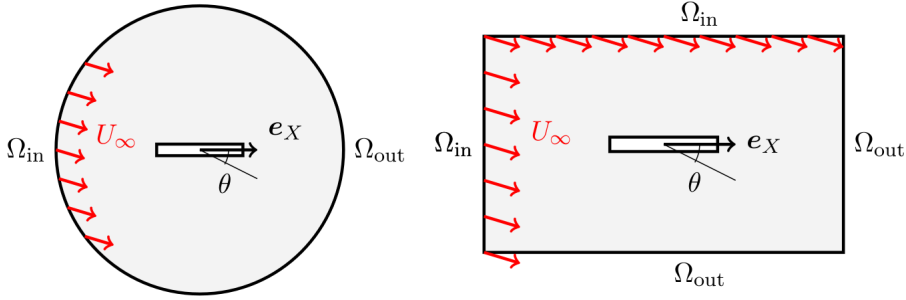
FIG. 15. Schemes of two cases modeling an equivalent situation to Fig. 1. (Left) Spherical grid labeled *mesh 2*. (Right) Cartesian grid with an inclined flow direction, labeled *mesh 3*. Ω_{in} and Ω_{out} represent, respectively, the inlet and outlet boundary conditions.

1. Investigation on the mesh quality

In our modeling strategy, we incline the cylinder relatively to the coordinate axes and background grid created by the `blockMesh` utility, while the inlet flow stays horizontal (see Fig. 1). For vertical and horizontal cylinders the mesh generated by `snappyHexMesh` is of good quality. In those cases, the cylinder surface is indeed parallel to the background grid, thus resulting in fewer skewed and nonorthogonal cells around the surface of the cylinder. Nonetheless, for a cylinder oriented with other angles of deviation, the cells near its surface are inevitably nonorthogonal, skewed, and nonhexahedral. For this reason, we present here a comparison between the mesh used in this work and two others types of meshes that result to cells of better quality.

Figure 15 displays a scheme of two different mesh configurations which are equivalent to the original one used in the main body of the paper. The first configuration, inspired from the study of Gao *et al.* [28], and exhibited in Fig. 15 (left), uses a fully hexahedral grid with a butterfly topology near the cylinder up to a spherical far-field topology. It has few skewed and nonorthogonal cells. We built this mesh with the software Pointwise. Half of the sphere domain is an inlet boundary condition, the other half corresponds to the outlet of the domain.

The second model, presented in Fig. 15 (right), is nearly the same as the original of Fig. 1, except that we kept the cylinder parallel to the background grid lines, as it was shown to yield a better quality of cells. The left and top boundaries are considered as inlets, while the bottom and right boundaries are outlets. In the direction perpendicular to the plane of Fig. 15, the front and back boundary conditions are zero-gradient. This enables us to incline the inlet flow direction instead of inclining the cylinder, and therefore preserve a good mesh quality. The outlet boundary condition corresponds to the following mathematical constrains, $\frac{\partial \mathbf{u}}{\partial \mathbf{n}} = \mathbf{0}$ for the velocity field and $p = 0$ for the pressure field, where $\mathbf{n}$ represents the outward normal to the boundary. The front and back boundary conditions are treated similarly to Sec. II, i.e., with zero-gradient conditions for all variables.

In the following, we will refer to the original model as *mesh 1*, the Pointwise mesh [Fig. 15 (left)] as *mesh 2*, and the last mesh [Fig. 15 (right)] will be referred as *mesh 3*.

On Table I, we display the main characteristics of the meshes namely, the maximum nonorthogonality factor, the maximum skewness factor, and the number of nonhexahedral cells in the mesh. Those characteristics are computed with the `checkMesh` utility of OpenFOAM and are of main importance to maintain consistency in the discretization of the Navier-Stokes equations [29]. *mesh 2* contains only hexahedral cells. Besides, it has an acceptable nonorthogonality and skewness coefficient and possesses a very high level of refinement with 113 cells per diameter. The *mesh 3* has the lowest maximum skewness and nonorthogonality factor but contains nonhexahedral cells (near the surface of the cylinder). *mesh 1* contains slightly more skewed, nonorthogonal and nonhexahedral cells. Consequently, our initial mesh *mesh 1* must perform as well as the other two models to be correctly validated.

TABLE I. Characteristics of each mesh. The nonorthogonality and skewness factors are computed with the `checkMesh` utility of OpenFOAM®.

	mesh 1	mesh 2	mesh 3
Maximum nonorthogonality factor	55.731	46.125	32.125
Maximum skewness factor	2.296	1.00	0.526
Number of nonhexahedral cells	49096	0	47256
Number of cells per diameter	30	113	30

We were able to perform a set of simulations at $\chi = 5$ and $\theta = 30$ for each mesh configuration, and for several Reynolds numbers. Additionally, we tried two gradient schemes, the Gauss linear (or Green-Gauss Cell-Based gradient scheme) and the Least Square gradient scheme. Figure 16 demonstrates without ambiguity that all meshes produce identical results when using a Gauss Linear scheme. Indeed, Fig. 16 shows a perfect agreement among all meshes for the drag and lift force, except for the *mesh 1* when using the Least Square gradient scheme represented by the "+" symbol in the graphs. This is not surprising as solely the original model contains a nonnegligible amount of nonorthogonal and skewed cells at the surface of the cylinder. As a consequence, the discretization using the Least Square scheme, leads ultimately to numerical errors. Which is nicely corrected with the use of the Gauss linear scheme. For further explanations on the Least square and Gauss linear scheme performance, we encourage the reader to look at the study of Syrakos *et al.* [29]. Note that other gradient schemes have been put to the test, such as the weighted least square and the point cells least square, but the most efficient was found to be the Gauss Linear gradient scheme. We must conclude that the meshes generated by `snappyHexMesh` perform as well as the Pointwise® mesh, despite the objectively less good quality of the cells generated all over the surface of the cylinder. Also, the perfect agreement on the drag and lift force between *mesh 1* and *mesh 2*, which possesses a definition of respectively 30 and 113 cells per diameter length, proves that our mesh is refined enough to capture the hydrodynamic stress on its surface (additional independence studies on the mesh refinement can be found in Fintzi [16]).

One last detail needs to be commented on the lift forces results, for Re < 0.1: we can notice that *mesh 3* overestimates the lift force compared to the two other meshes. We observed these slight variations in the results only at low Reynolds numbers. We determined that the differences are due
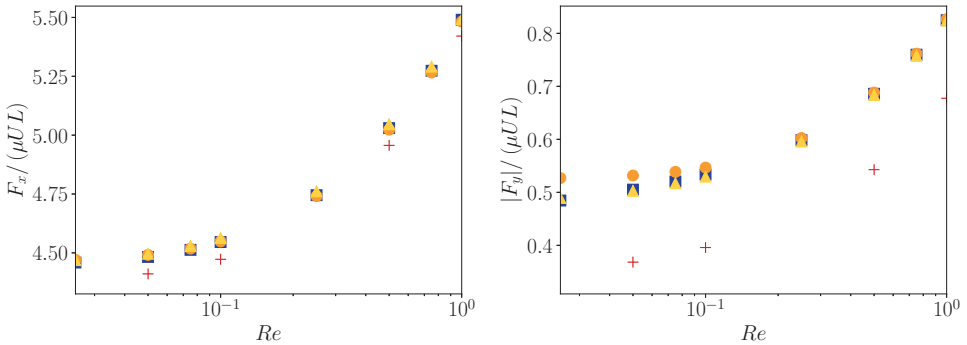

FIG. 16. (left) Dimensionless drag force F_x. (right) Dimensionless lift force F_y. The aspect ratio and angle of incidence considered are, $\chi = 5$ and $\theta = 30°$. (■) Simulations performed on the original model, *mesh 1*, presented Fig. 1 with a Gauss Linear gradient scheme. (+) Simulation performed on *mesh 1* but with Least Square gradient scheme. (▲) Pointwise® butterfly topology mesh [see *mesh 2* in Fig. 15 (left)]. (●) Orthogonal grid with leaned flow input direction [see *mesh 3* in Fig. 15 (right)].
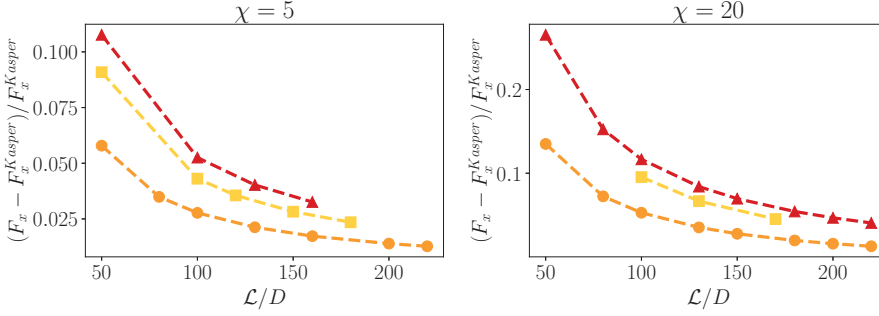
FIG. 17. Relative error between the numerical results and experimental results of Kasper *et al.* [19] for the drag force applied on a cylinder translating perpendicular to the flow at Re = 0.01. The error is shown versus the domain size $\mathcal{L}/D$ for the different boundary conditions on the domain sides. ▲: Dirichlet; ■: Symmetry; ●: Neumann.

to the use of different boundary conditions, specifically the two inlet Dirichlet boundaries in this case, instead of the Neumann boundary condition prescribed on the side of *mesh 1*.

2. Influence of the domain size and boundary conditions

Having considered the key points from the last subsection, we now examine the influence of the domain size and boundary conditions on the accuracy of the results by a comparison with experimental data. We consider a perpendicularly oriented cylindrical particle translating at constant velocity. To determine the optimal size of the domain, we make a parametric study by changing the domain size $\mathcal{L}$. In each of those cases, we will evaluate the normalized drag force along the $\mathbf{e}_x$ axis and compare that force to the reference Kasper *et al.* [19]. The choice of boundary condition at far-field is subjective, since the initial problem is supposed to have no boundary at all. We investigated different setups of boundary conditions. All the cases studied here share the same boundary condition on the inlet and outlet of the domain, i.e., a Dirichlet boundary condition for the velocity and a null pressure gradient at inlet, in combination with a null pressure field and a null velocity gradient at outlet. Our first try, called Dirichlet in the following, is to impose $\mathbf{u} = U\mathbf{e}_x$ and $p = 0$ on the side boundaries. We can also impose a null gradient for both variables on all the sides of the domain, i.e., $\partial \mathbf{u}/\partial \mathbf{n} = \mathbf{0}$ and $\partial p/\partial \mathbf{n} = 0$. We call this condition Neumann. Likewise, we can impose symmetry boundary conditions, that we will call Symmetry, such that $\partial p/\partial \mathbf{n} = 0$, $u_n = 0$ and $\partial u_t/\partial \mathbf{n} = 0$ on the sides, where u_t is the tangential component of the velocity and u_n the normal component. We have also carried out a parametric analysis of the size of the domain relative to the cylinder diameter.

In Fig. 17, we can observe that regardless the boundary condition type, i.e., Neumann and Dirichlet and Symmetry, all cases tend toward the reference value as $\mathcal{L}/D$ tends to infinity. This proves that our numerical strategy is able to converge to the experimental results at the expense of large computational domains. Furthermore, we can see that the Neumann set of boundary conditions has the smallest relative error with respect to the other boundary conditions. Hence, we have chosen in this study to select the Neumann boundary conditions on all our side boundaries. Also, a domain size $\mathcal{L} \approx (100 + 5\chi)D$ is sufficient to avoid significant effects of the boundaries on the numerical results up to $\chi = 20$.

APPENDIX B: SLENDER-BODY THEORY

1. Loads on a slender cylinder oriented arbitrarily in a uniform flow

In their original article, the authors of Ref. [7] performed a matched asymptotic expansion in $1/\ln(\chi)$ assuming $\chi \ll 1$. For bodies with a straight centreline, they were able to obtain the force

per unit of length. In the case of a straight cylinder of circular cross-section the force per unit of length reads

$$
\begin{aligned}
\frac{\mathbf{f}(s)}{2\pi\mu U} = &-\left(\frac{1}{\ln\chi}\right)(\cos\theta\,\mathbf{p}-2\mathbf{e_x})+\left(\frac{1}{\ln\chi}\right)^2\left\{\frac{1}{4}[2\cos\theta\,\mathbf{e_x}-(2-\cos\theta+\cos^2\theta)\mathbf{p}]\right.\\
&\times\left[\frac{1-e^{-X}}{X}-1\right]-\frac{1}{4}[2\cos\theta\,\mathbf{e_x}-(2+\cos\theta+\cos^2\theta)\mathbf{p}]\left[\frac{1-e^{Y}}{Y}-1\right]\\
&-\frac{1}{2}(\cos\theta\,\mathbf{p}-2\mathbf{e_x})[E_1(X)+\ln(1-\cos\theta)]-\frac{1}{2}(\cos\theta\,\mathbf{p}-2\mathbf{e_x})[E_1(Y)+\ln(1+\cos\theta)]\\
&\left.-(\cos\theta\,\mathbf{p}-2\mathbf{e_x})\left(\gamma+\ln\left(\frac{1}{4}\mathrm{Re}_L\right)\right)+\frac{3}{2}\cos\theta\,\mathbf{p}-\mathbf{e_x}\right\}+\mathcal{O}\left(\frac{1}{\ln\chi}\right)^3,
\end{aligned}
\tag{B1}
$$

where $X=\frac{1}{2}\mathrm{Re}_L(1-\cos\theta)(1+s)$, $Y=\frac{1}{2}\mathrm{Re}_L(1+\cos\theta)(1-s)$, γ is the Euler's constant, and $E_1(x)$ is the exponential integral function. Using the expression above, the force and torque acting on the body can be readily obtained as $\mathbf{F}=L/2\int_{-1}^{1}\mathbf{f}(s)ds$ and $\mathbf{T}=L^2/4\mathbf{p}\times\int_{-1}^{1}s\mathbf{f}(s)ds$. By performing the integration, Khayat and Cox [7] derived three main formulas describing the loads on a cylinder inclined by an angle of θ with respect to the flow direction. Those formulas are written below in terms of our parameters and the Reynolds number based on the length of the cylinder, $\mathrm{Re}_L=\chi\mathrm{Re}/2$. The drag force F_x, the lift force F_y, and the torque T_z read

$$
\frac{F_x(\mathrm{Re},\theta)}{\mu UL}=\frac{-2\pi(2-\cos^2\theta)}{-\ln\chi+D(\mathrm{Re}_L=0,\theta)}\left(1+\frac{D(\mathrm{Re}_L,\theta)-D(\mathrm{Re}_L=0,\theta)}{\ln\chi}\right)+\mathcal{O}\left(\frac{1}{\ln\chi}\right)^3,\tag{B2}
$$

$$
\frac{F_y(\mathrm{Re},\theta)}{\mu UL}=\frac{\pi\sin 2\theta}{-\ln\chi+L(\mathrm{Re}_L=0,\theta)}\left(1+\frac{L(\mathrm{Re}_L,\theta)-L(\mathrm{Re}_L=0,\theta)}{\ln\chi}\right)+\mathcal{O}\left(\frac{1}{\ln\chi}\right)^3,\tag{B3}
$$

$$
\frac{T_z(\mathrm{Re},\theta)}{\mu UL^2}=-\frac{1}{2}\pi\left(\frac{1}{\ln\chi}\right)^2 G(\mathrm{Re}_L,\theta)+\mathcal{O}\left(\frac{1}{\ln\chi}\right)^3.\tag{B4}
$$

Note that we have preferred the expressions (6.14) and (6.15) to (6.8) and (6.10) in Khayat and Cox [7], since the latter diverges as Re_L tends to infinity. Expressions for $D(\mathrm{Re}_L,\theta)$, $L(\mathrm{Re}_L,\theta)$, and $G(\mathrm{Re}_L,\theta)$ are detailed below:

$$
\begin{aligned}
D(\mathrm{Re}_L,\theta)=&\left(\frac{\cos^2\theta}{2\mathrm{Re}_L}(C(X)+C(Y))+3\cos^2\theta-2\right)\frac{1}{2(2-\cos^2\theta)}+B(X)+B(Y)\\
&+\frac{1}{2}\ln(1-\cos^2\theta)+\gamma+\ln\left(\frac{\mathrm{Re}_L}{4}\right)
\end{aligned}
$$

$$
\begin{aligned}
L(\mathrm{Re}_L,\theta)=&\left[\left(\frac{(2-\cos\theta+\cos^2\theta)\sin\theta}{2X}\right)C(X)-\left(\frac{(2+\cos\theta+\cos^2\theta)\sin\theta}{2Y}\right)C(Y)\right]\frac{1}{\sin(2\theta)}\\
&-\frac{3}{2}+B(X)+B(Y)+\frac{1}{2}\ln(1-\cos^2\theta)+\gamma+\ln\left(\frac{\mathrm{Re}_L}{4}\right)
\end{aligned}
$$

$$
G(\mathrm{Re}_L,\theta)=[\cos\theta(P(X)-Q(X)+P(Y)-Q(Y))+P(Y)-P(X)]\sin\theta
$$

with $C(x)=E_1(x)+\ln(x)+\gamma-x$, $Z(x)=\frac{e^{-x}-1}{x}$, $B(x)=\frac{1}{2}(E_1(x)-Z(x))$, $Q(x)=\frac{E_1(x)+\ln(x)+\gamma}{x}$, $P(x)=\frac{2}{x}(1+\frac{e^{-x}-1}{x})$, $X=\mathrm{Re}_L(1-\cos\theta)$ and $Y=\mathrm{Re}_L(1+\cos\theta)$.

2. Switching from a $1/\ln(\chi)$ expansion to a $1/\ln(2\chi)$ expansion

Let us define $f(\chi)$ an arbitrary expansion of order l in $1/\ln(\chi)$,

$$f(\chi) = \sum_{n=1}^{l} \frac{a_n}{\ln^n(\chi)} + \mathcal{O}\left(\frac{1}{\ln(\chi)}\right)^{l+1}, \tag{B5}$$

where a_n are the series coefficients. We aim at finding the corresponding coefficients, b_n, such that

$$f(\chi) = \sum_{n=1}^{l} \frac{a_n}{\ln^n(\chi)} + \mathcal{O}\left(\frac{1}{\ln(\chi)}\right)^{l+1} = \sum_{n=1}^{l} \frac{b_n}{\ln^n(2\chi)} + \mathcal{O}\left(\frac{1}{\ln(2\chi)}\right)^{l+1}. \tag{B6}$$

We start by considering only one term $1/\ln^n(\chi)$ which can be expressed as

$$\frac{1}{\ln^n(\chi)} = \frac{1}{\ln^n(2\chi)}\left[1 + \left(1 - \frac{\ln(2)}{\ln(2\chi)}\right)^n - 1\right]^{-1} \tag{B7}$$

$$= \frac{1}{\ln^n(2\chi)}\sum_{i=0}^{\infty}\left[1 - \left(1 - \frac{\ln(2)}{\ln(2\chi)}\right)^n\right]^i \tag{B8}$$

$$= \frac{1}{\ln^n(2\chi)}\sum_{i=0}^{\infty}\sum_{j=0}^{i}\binom{i}{j}(-1)^j\left(1 - \frac{\ln(2)}{\ln(2\chi)}\right)^{nj} \tag{B9}$$

$$= \frac{1}{\ln^n(2\chi)}\sum_{i=0}^{\infty}\sum_{j=0}^{i}\sum_{k=0}^{nj}\binom{i}{j}\binom{nj}{k}(-1)^{j+k}\frac{\ln^k(2)}{\ln^k(2\chi)}, \tag{B10}$$

where we have used the infinite series $1/(1 - X) = \sum_{i=0}^{\infty} X^n$ and the binomial theorem. If we substitute Eq. (B10) into Eq. (B5), then we obtain

$$f(\chi) = \sum_{n=1}^{l} \frac{a_n}{\ln^n(\chi)} = \sum_{n=1}^{l}\sum_{i=0}^{l-n}\sum_{j=0}^{i}\sum_{k=0}^{nj} a_n\binom{i}{j}\binom{nj}{k}(-1)^{j+k}\frac{\ln^k(2)}{\ln^{k+n}(2\chi)} + \mathcal{O}\left(\frac{1}{\ln(\chi)}\right)^{l+1}. \tag{B11}$$

In particular,

$$\frac{a_1}{\ln(\chi)} + \frac{a_2}{\ln^2(\chi)} + \frac{a_3}{\ln^3(\chi)} + \frac{a_4}{\ln^4(\chi)} = \frac{b_1}{\ln(2\chi)} + \frac{b_2}{\ln^2(2\chi)} + \frac{b_3}{\ln^3(2\chi)} + \frac{b_4}{\ln^4(2\chi)}$$

$$+ \mathcal{O}\left(\frac{1}{\ln(2\chi)}\right)^5, \tag{B12}$$

with $b_1 = a_1$, $b_2 = \ln(2)a_1 + a_2$, $b_3 = \ln^2(2)a_1 + 2\ln(2)a_2 + a_3$, and $b_4 = \ln^3(2)a_1 + 3\ln^2(2)a_2 + 3\ln(2)a_3 + a_4$. Similar calculations lead to the formula to switch from a $1/\ln(2\chi)$ expansion to a $1/\ln(\chi)$ expansion,

$$f(\chi) = \sum_{n=1}^{l} \frac{b_n}{\ln^n(2\chi)} = \sum_{n=1}^{l}\sum_{i=0}^{l-n}\sum_{j=0}^{i}\sum_{k=0}^{nj} b_n\binom{i}{j}\binom{nj}{k}(-1)^j\frac{\ln^k(2)}{\ln^{k+n}(\chi)} + \mathcal{O}\left(\frac{1}{\ln(\chi)}\right)^{l+1}. \tag{B13}$$

3. Higher-order slender body prediction for the drag force on a cylinder aligned with the flow direction

In their study, Khair and Chisholm [8] derived the third-order inertial contribution to the drag force on an axisymmetric body aligned with the flow direction. Although their formulas are very general, they did not derive in closed form the analytical expression for a cylindrical body. This is the purpose of the present Appendix. Khair and Chisholm [8] have decomposed the third-order inertial
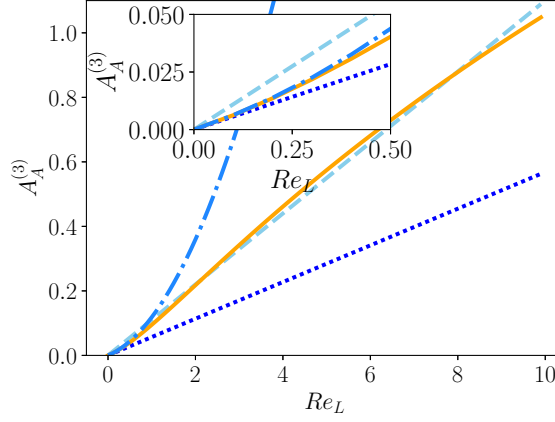
FIG. 18. Plot of $A_A^{(3)}$ versus Re_L. Solid line (−): numerical integration of Eq. (B14); dashed lines (−−): Eq. (B16); dotted line (··): $A_A^{(3)}(\mathrm{Re}_L) = (\frac{3}{4} - \ln 2)\mathrm{Re}_L$; dashed-dotted line (− · −): Eq. (B15).

$A^{(3)}(\mathrm{Re}_L)$ term into two parts, $A_A^{(3)}(\mathrm{Re}_L)$ and $A_B^{(3)}(\mathrm{Re}_L)$. After some algebra, the first contribution reads for a cylindrical body

$$A_A^{(3)}(\mathrm{Re}_L) = \int_{-1}^{1} f_A^{(3)}(z, \mathrm{Re}_L)d_z, \tag{B14}$$

with

$$f_A^{(3)}(z, \mathrm{Re}_L) = \pi \left\{ E_1[\mathrm{Re}_L(1-z)] + \frac{-z\mathrm{Re}_L + e^{\mathrm{Re}_L(z-1)} + \mathrm{Re}_L - 1}{\mathrm{Re}_L(z-1)} + \ln[\mathrm{Re}_L(1-z)] + \gamma \right\}$$

$$\times \left\{ E_1(\mathrm{Re}_L - \mathrm{Re}_L z) + \frac{e^{\mathrm{Re}_L(z-1)}}{\mathrm{Re}_L(z-1)} + \frac{1}{\mathrm{Re}_L(1-z)} + \ln[\mathrm{Re}_L(1-z)] \right.$$

$$\left. - 4\ln(2\sqrt{1-z^2}) + \gamma + 1 \right\}.$$

Note that the normalization of the force differs by a factor of 2 between Khair and Chisholm [8] and our present convention. As Khair and Chisholm [8] for spheroidal particle, we were unable to obtain the integral (B14) in closed form. However, we can gain further insight into the integral by expanding f_{3A} in the limit $\mathrm{Re}_L \ll 1$,

$$f_A^{(3)}(\mathrm{Re}_L, z) = \pi \mathrm{Re}_L(z-1)[2\ln(2\sqrt{1-z^2}) - 1] + \pi \mathrm{Re}_L^2 \left\{ \frac{1}{4}(1-z)^2 - \frac{1}{12}(z-1)^2 \right.$$

$$\left. \times [2 - 4\ln(2\sqrt{1-z^2})] \right\} + \mathcal{O}(\mathrm{Re}_L^3).$$

After integration, we obtain the following expression for $A_A^{(3)}$

$$A_A^{(3)}(\mathrm{Re}_L) = \left(\frac{3}{4} - \ln 2\right)\mathrm{Re}_L + \left(\frac{2}{9}\ln 2 - \frac{5}{54}\right)\mathrm{Re}_L^2 + \mathcal{O}(\mathrm{Re}_L^3). \tag{B15}$$

As expected, $A_A^{(3)}$ is an inertial correction since it is zero for $\mathrm{Re}_L = 0$. Also, as observed by Khair and Chisholm [8] for spheroids, the leading-order term in the expansion grows as Re. In contrast to what Khair and Chisholm [8] reported for spheroid, $A_A^{(3)}(\mathrm{Re}_L)$ is positive for cylindrical particle while it is negative up to $\mathrm{Re}_L \approx 5$ for spheroid.

We have also carried out the integration of Eq. (B14) numerically which is represented in Fig. 18. Equation (B15) is valid up to $\mathrm{Re}_L \approx 0.5$, while its first-order linear approximation ceases to be valid at Re ≈ 0.25. As can be observed, the integral can be reasonably approximated by the following
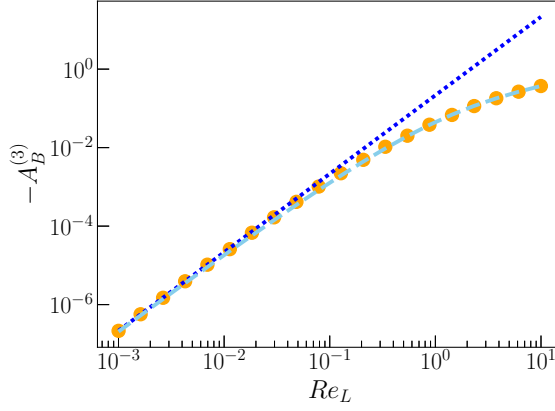
FIG. 19. Plot of $A_B^{(3)}$ versus Re_L. ($\circ$): numerical quadrature [8]; dashed lines ($--$): Eq. (B17); dotted line ($\cdot\cdot$): $0.215\mathrm{Re}_L^2$.

linear function over the whole range of Re_L investigated (except for $\mathrm{Re}_L \leqslant 0.5$ where both Taylor expansions are more accurate),

$$A_A^{(3)} = 0.11\mathrm{Re}_L. \tag{B16}$$

Thus, we choose to keep the simple but efficient linear fit to represent $A_A^{(3)}$.

As stated in Khair and Chisholm [8], $A_B^{(3)}$ is independent of the body shape. Khair and Chisholm [8] expressed $A_B^{(3)}$ in the Fourier space and they also performed a numerical quadrature to express it in the real space. Their result is displayed in Fig. 19. It is possible to fit the numerical results given in Khair and Chisholm [8], which gives us the following expression for the total inertial term

$$A_B^{(3)}(\mathrm{Re}_L) = -\frac{0.215\log\left(\mathrm{Re}_L^{1.26} + 1\right)}{\mathrm{Re}_L^{1.26}\mathrm{Re}_L^{-2} + 2.341\mathrm{Re}_L^{-0.184}}, \tag{B17}$$

which tends toward $-0.215\mathrm{Re}_L^{-2}$ as Re_L tends toward zero.

[1] M. Cole, A novel method for preparing microplastic fibers, Sci. Rep. **6**, 1 (2016).

[2] P. Anand, S. S. Ray, and G. Subramanian, Orientation Dynamics of Sedimenting Anisotropic Particles in Turbulence, Phys. Rev. Lett. **125**, 034501 (2020).

[3] N. Pujara, G. A. Voth, and E. A. Variano, Scale-dependent alignment, tumbling, and stretching of slender rods in isotropic turbulence, J. Fluid Mech. **860**, 465 (2019).

[4] G. K. Batchelor, Slender-body theory for particles of arbitrary cross-section in stokes flow, J. Fluid Mech. **44**, 419 (1970).

[5] R. Cox, The motion of long slender bodies in a viscous fluid part 1. General theory, J. Fluid Mech. **44**, 791 (1970).

[6] R. Cox, The steady motion of a particle of arbitrary shape at small Reynolds numbers, J. Fluid Mech. **23**, 625 (1965).

[7] R. Khayat and R. Cox, Inertia effects on the motion of long slender bodies, J. Fluid Mech. **209**, 435 (1989).

[8] A. S. Khair and N. G. Chisholm, A higher-order slender-body theory for axisymmetric flow past a particle at moderate Reynolds number, J. Fluid Mech. **855**, 421 (2018).

[9] D. Lopez and E. Guazzelli, Inertial effects on fibers settling in a vortical flow, Phys. Rev. Fluids **2**, 024306 (2017).

[10] A. Roy, R. J. Hamati, L. Tierney, D. L. Koch, and G. A. Voth, Inertial torques and a symmetry breaking orientational transition in the sedimentation of slender fibres, J. Fluid Mech. **875**, 576 (2019).

[11] F. Cabrera, M. Z. Sheikh, B. Mehlig, N. Plihon, M. Bourgoin, A. Pumir, and A. Naso, Experimental validation of fluid inertia models for a cylinder settling in a quiescent flow, Phys. Rev. Fluids **7**, 024301 (2022).

[12] A. Vakil and S. I. Green, Drag and lift coefficients of inclined finite circular cylinders at moderate Reynolds numbers, Comput. Fluids **38**, 1771 (2009).

[13] M. Kharrouba, J.-L. Pierson, and J. Magnaudet, Flow structure and loads over inclined cylindrical rodlike particles and fibers, Phys. Rev. Fluids **6**, 044308 (2021).

[14] M. Shin, D. L. Koch, and G. Subramanian, A pseudospectral method to evaluate the fluid velocity produced by an array of translating slender fibers, Phys. Fluids **18**, 063301 (2006).

[15] OpenCFD, *OpenFOAM, The Open Source CFD Toolbox, User Guide. Version v2206* (ESI, 2022).

[16] N. Fintzi, Towards generalized hydrodynamic stress models for cylindrical particles, either isolated or in packed beds, Master thesis, INSA Lyon, 2021.

[17] E. Guazzelli and J. F. Morris, *A Physical Introduction to Suspension Dynamics* (Cambridge University Press, Cambridge, UK, 2011), Vol. 45.

[18] F. Jiang, L. Zhao, H. I. Andersson, K. Gustavsson, A. Pumir, and B. Mehlig, Inertial torque on a small spheroid in a stationary uniform flow, Phys. Rev. Fluids **6**, 024302 (2021).

[19] G. Kasper, T. Niida, and M. Yang, Measurements of viscous drag on cylinders and chains of spheres with aspect ratios between 2 and 50, J. Aerosol Sci. **16**, 535 (1985).

[20] T. Ui, R. Hussey, and R. Roger, Stokes drag on a cylinder in axial motion, Phys. Fluids **27**, 787 (1984).

[21] S. Kim and S. J. Karrila, *Microhydrodynamics: Principles and selected applications* (Courier Corporation, Chelmsford, MA, 2013).

[22] H. Brenner and R. Cox, The resistance to a particle of arbitrary shape in translational motion at small Reynolds numbers, J. Fluid Mech. **17**, 561 (1963).

[23] J.-L. Pierson, F. Auguste, A. Hammouti, and A. Wachs, Inertial flow past a finite-length axisymmetric cylinder of aspect ratio 3: Effect of the yaw angle, Phys. Rev. Fluids **4**, 044802 (2019).

[24] G. Subramanian and D. L. Koch, Inertial effects on fibre motion in simple shear flow, J. Fluid Mech. **535**, 383 (2005).

[25] R. Newsom and C. Bruce, The dynamics of fibrous aerosols in a quiescent atmosphere, Phys. Fluids **6**, 521 (1994).

[26] J.-L. Pierson, M. Kharrouba, and J. Magnaudet, Hydrodynamic torque on a slender cylinder rotating perpendicularly to its symmetry axis, Phys. Rev. Fluids **6**, 094303 (2021).

[27] J. Teng, B. Rallabandi, H. A. Stone, and J. T. Ault, Coupling of translation and rotation in the motion of finite-length rods near solid boundaries, J. Fluid Mech. **938**, A30 (2022).

[28] S. Gao, L. Tao, X. Tian, and J. Yang, Flow around an inclined circular disk, J. Fluid Mech. **851**, 687 (2018).

[29] A. Syrakos, S. Varchanis, Y. Dimakopoulos, A. Goulas, and J. Tsamopoulos, A critical analysis of some popular methods for the discretisation of the gradient operator in finite volume methods, Phys. Fluids **29**, 127103 (2017).